HHS Public Access

Author manuscript

Immunity. Author manuscript; available in PMC 2021 August 18.

Published in final edited form as:

Immunity. 2020 August 18; 53(2): 398–416.e8. doi:10.1016/j.immuni.2020.07.010.

Paneth cell-derived lysozyme defines the composition of mucolytic microbiota and the inflammatory tone of the intestine

Shiyan Yu[1,13,#], **Iyshwarya Balasubramanian**[1,13], **Daniel Laubitz**[2], **Kevin Tong**[3], **Sheila Bandyopadhyay**[1], **Xiang Lin**[4], **Juan Flores**[1], **Rajbir Singh**[1], **Yue Liu**[1], **Carlos Macazana**[1], **Yanlin Zhao**[5], **Fabienne Béguet-Crespel**[6], **Karuna Patil**[2], **Monica T Midura-Kiela**[2], **Daniel Wang**[1], **George S. Yap**[5], **Ronaldo P. Ferraris**[7], **Zhi Wei**[4], **Edward M. Bonder**[1], **Max M. Häggblom**[8], **Lanjing Zhang**[1,9], **Veronique Douard**[6], **Michael P. Verzi**[3], **Ken Cadwell**[10], **Pawel R. Kiela**[2,11], **Nan Gao**[1,12,*]

[1]Department of Biological Sciences, Rutgers University, Newark, NJ, USA.

[2]Department of Pediatrics, University of Arizona, Tucson, AZ, USA.

[3]Department of Genetics, Rutgers University, Piscataway, NJ, USA.

[4]Department of Computer Science, New Jersey Institute of Technology, Newark, NJ, USA.

[5]Center for Immunity and Inflammation, Rutgers New Jersey Medical School, Newark, NJ, USA.

[6]Micalis Institute, Institut National de la Recherche Agronomique (INRA), AgroParisTech, Université Paris-Saclay, Jouy-en-Josas, France.

[7]Department of Pharmacology, Physiology and Neuroscience, Rutgers New Jersey Medical School, Newark, NJ, USA.

[8]Department of Biochemistry and Microbiology, Rutgers University, New Brunswick, NJ, USA.

[9]Department of Pathology, Princeton Medical Center, Plainsboro, NJ, USA.

[10]Department of Microbiology and Kimmel Center for Biology and Medicine at the Skirball Institute, New York University School of Medicine, NY, USA.

[11]Department of Immunobiology, University of Arizona, Tucson, AZ, USA.

[12]Rutgers Cancer Institute of New Jersey, New Brunswick, NJ, USA

[13]Shiyan Yu and Iyshwarya Balasubramanian contributed equally to this work.

[*]Corresponding author and Lead contact: Nan Gao, Ph.D., ngao@newark.rutgers.edu.

[#]Current Affiliation- Shanghai Institute of Precision Medicine, Ninth People's Hospital, Shanghai Jiao Tong University School of Medicine, Shanghai, China

AUTHOR CONTRIBUTIONS

S.Y., I.B., G.S.Y., K.C, P.R.K, N.G. formulated the hypothesis, conceptualized the idea, designed research; S.Y., I.B., N.G. wrote the manuscript; S.Y., I.B., D.L., K.T., S.B., J.F., R.S., Y.L., C.M., Y.Z., F.B.C., K. P., M.T.M-K., D.W., R.P.F., E.M.B., M.H., L.Z., V.D., M.P.V. performed experiments, analyzed and reported data.

DECLARATION OF INTERESTS

The authors declare no competing interests.

SUMMARY

Paneth cells are the primary source of C-type lysozyme, a β−1,4-N-acetylmuramoylhydrolase that enzymatically processes bacterial cell walls. Paneth cells are normally present in human cecum and ascending colon, but are rarely found in descending colon and rectum; Paneth cell metaplasia in this region and aberrant lysozyme production are hallmarks of IBD pathology. Here we examined the impact of aberrant lysozyme production in colonic inflammation. Targeted disruption of Paneth cell lysozyme (*Lyz1*) protected mice from experimental colitis. *Lyz1*-deficiency diminished intestinal immune responses to bacterial molecular patterns and resulted in the expansion of lysozyme-sensitive mucolytic bacteria, including *Ruminococcus gnavus, a* Crohn's disease-associated pathobiont. Ectopic lysozyme production in colonic epithelium suppressed lysozyme-sensitive bacteria and exacerbated colitis. Transfer of *R. gnavus* into $Lyz1^{-/-}$ hosts elicited a type 2 immune response, causing epithelial reprograming and enhanced anti-colitogenic capacity. In contrast, in lysozyme-intact hosts, processed *R. gnavus* drove pro-inflammatory responses. Thus, Paneth cell lysozyme balances intestinal anti- and pro-inflammatory responses, with implications for IBD.

eTOC Blurb

Paneth cell metaplasia to the colon and rectum and aberrant lysosome production are hallmarks of inflammatory bowel disease in humans. Using mouse models were *Lyz1* is deleted or ectopically expressed, Yu, Balasubramanian et al show that Paneth cell lysozyme regulates the abundance of mucolytic commensal bacteria and thereby the intestinal inflammatory response.

Graphical Abstract

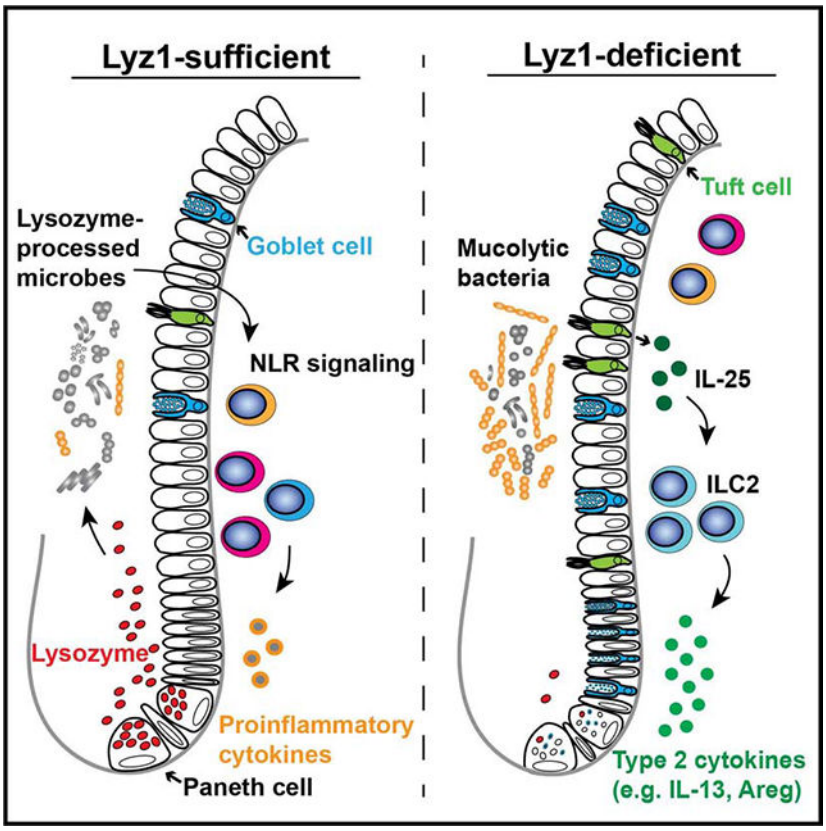

Keywords

Lysozyme; Paneth cell; Type 2 immunity; Colitis; Lyz1; Ruminococcus gnavus

INTRODUCTION

Intestinal Paneth cells and certain myeloid cells produce the C-type lysozyme, a β−1,4-N-acetylmuramoylhydrolase that enzymatically processes bacterial cell walls. The products of lysozyme processing, such as muramyl dipeptide (MDP) can be important agonists of pattern recognition receptors (PRR), notably NOD-like receptors (NLR) (Balasubramanian and Gao, 2017). Biochemical studies of lysozyme identified a helix-loop-helix bactericidal domain mediating its membrane-permeabilizing action (Canfield and Liu, 1965; Ibrahim et al., 2001b). It is distinct from lysozyme's enzymatic domain (Ibrahim, 1998), illustrating a unique dual functionality of lysozyme that distinguishes it from other antimicrobial peptides.

Paneth cells secrete lysozyme into the intestinal lumen (Bel et al., 2017), constituting the primary source of luminal lysozyme that directly encounters commensal bacteria. Macrophages and neutrophils are major sources of lysozyme within the intestinal lamina propria (LP). In humans, macrophage- and Paneth cell-derived lysozyme is encoded by a single *LYZ* gene on chromosome 12q15. This gene is located in the vicinity of an Ulcerative Colitis (UC) risk locus harboring *IFN-γ, IL26*, and *IL22* (Jostins et al., 2012; Silverberg et al., 2009). Hereditary *LYZ* mutation causes familial amyloidosis (Pepys et al., 1993) and

patients carrying mutant LYZ exhibit gastritis and inflammatory bowel disease (IBD) symptoms such as abdominal pain, malabsorption, diarrhea, and weight loss (Girnius et al., 2012; Jean et al., 2014).

Whereas Paneth cells are absent in rodent colonic epithelium, these cells are normally present in human cecum and ascending (i.e., right) colon. However, they are rarely found in human descending colon and rectum and Paneth cell metaplasia in this region is a hallmark of IBD pathology (Singh et al., 2020; Tanaka et al., 2001). Clinical studies demonstrated a correlation between aberrant lysozyme production and IBD. Increased fecal lysozyme was reported in UC patients over 70 years ago (Meyer et al., 1947, 1948). Subsequent studies suggested that fecal and blood lysozyme levels are excellent indicators for IBD activity (Di Ruscio et al., 2017; Klass and Neale, 1978). Colonic epithelia of UC patients exhibit elevated expression of lysozyme messenger (m)RNA and protein, primarily in metaplastic Paneth-like cells (Fahlgren et al., 2003), which has been speculated to represent the host's attempt to control the increased bacterial adherence to the intestinal epithelial cell (IEC) surface. Paneth cells in Crohn's Disease (CD) patients with polymorphisms in *ATG16L1 (T300A)* or *NOD2* alleles exhibit aberrant lysozyme packaging, with lysozyme-containing secretory granules abnormally dispersed within the cytoplasm or degraded (Cadwell et al., 2008; VanDussen et al., 2014). This aberrant lysozyme granular morphology in Paneth cells is predictive of the timing of CD recurrence after surgery (Liu et al., 2017; VanDussen et al., 2014). Another major CD susceptibility gene product, Leucine-Rich Repeat Kinase 2 (LRRK2), selectively packages lysozyme but not REG3 or defensins into the dense core secretory granules in Paneth cells (Zhang et al., 2015). Loss of LRRK2 results in lysozyme mis-trafficking and degradation, a deficiency speculated to be responsible for the increased *Listeria monocytogenes* invasion in *Lrrk2*$^{-/-}$ mice (Zhang et al., 2015).

Although abnormal Paneth cell morphology and lysozyme production are observed in IBD pathology, whether aberrant lysozyme production per se impacts disease susceptibility has not been directly examined. Here we used multiple mouse models to address this question, and found that lysozyme produced by Paneth cells defined certain populations of gut commensal bacteria. Ectopic lysozyme production exacerbated experimental colitis, whereas lysozyme deficiency altered the mucosal immune profile via an altered bacterial landscape.

RESULTS

MDP and NLR signaling is diminished in the intestine of *Lyz1*$^{-/-}$ mice

The physiological function of intestinal luminal lysozyme is unclear. While normal human left colons do not have lysozyme-expressing Paneth cells, metaplastic Paneth cells in IBD patients' left colons expressed lysozyme (Fig. 1A, Fig. S1A, p=0.00012). Mouse *Lyz1* and *Lyz2* encode for lysozyme in Paneth cells and in leukocytes, respectively (Markart et al., 2004a). We targeted *Lyz1* (Yu et al., 2018), and developed *Lyz1*$^{-/-}$ mice to study the function of Paneth cell lysozyme. Loss of intestinal lysozyme in *Lyz1*$^{-/-}$ mice was confirmed at the level of mRNA (Fig. S1B), protein (Fig. 1B–C, Fig. S1C), and enzymatic activity (Fig. 1D). *Lyz1*$^{-/-}$ mice did not show changes in body weight or activity compared to their wild type (WT) littermates. All comparisons in this study were conducted among littermates.

Bulk RNA sequencing analysis of the ileum of adult WT and *Lyz1*$^{-/-}$ mice revealed 404 transcripts whose expression was increased and 447 transcripts whose expression was decreased in *Lyz1*$^{-/-}$ mice ($p<0.05$, Fig. S1D). *Lyz1* was abolished as expected (Fig. S1E). Kyoto Encyclopedia of Genes and Genomes (KEGG) analysis revealed the top 5 decreased modules in *Lyz1*$^{-/-}$ intestines to represent apoptosis, antigen presentation, NLR signaling, cytoplasmic PRR signaling, and RIG1-like receptor signaling ($p=0.0$, Fig. 1E). Gene Set Enrichment Analysis (GSEA) suggested that Paneth cell transcriptome was preserved in the *Lyz1*$^{-/-}$ ileum ($p>0.05$, Fig. 1F), a finding validated by the preserved expression of Paneth cell-specific markers such as Mmp7 (Fig. S1F). Signature gene sets for cytoplasmic PRR signaling (Fig. 1G), especially the NLR signaling (Fig. 1H, I), were reduced in *Lyz1*$^{-/-}$ intestines. We detected a reduced cellular response to MDP (Fig. 1J), likely reflecting a lack of lysozyme-processing of peptidoglycan. GSEA and gene ontology analysis further identified suppression of cytokine production, suppression of inflammatory response, and suppression of ROS signaling in *Lyz1*$^{-/-}$ intestines (Fig. 1K–L, Fig. S1G–H). Thus, *Lyz1* deficiency diminishes the intestinal mucosal response to bacterial molecular patterns.

Lyz1 deficiency ameliorated dextran sulfate sodium (DSS)-induced intestinal inflammation

Paneth cell-derived lysozyme is secreted into the intestinal lumen (Bel et al., 2017) and excreted with feces (Meyer et al., 1947, 1948). In line with this, lysozyme immunoreactivity was detected in WT adult mouse colonic lumen, and it was lost in *Lyz1*$^{-/-}$ mice (Fig. S1C). Given the correlation between lysozyme and intestinal inflammation, we then tested the impact of lysozyme deficiency on experimental colitis. DSS in drinking water induces colitis in mice (Okayasu et al., 1990). DSS administration in WT mice robustly elevated *Lyz1* and *Lyz2* expression in inflamed colons whereas the same treatment elevated *Lyz2* in *Lyz1*$^{-/-}$ mouse colons (Fig. S1I, J). Compared to WT littermates, colitis in *Lyz1*$^{-/-}$ mice was ameliorated, with rapid body weight recovery (Fig. 1M) and lower pathology scores (Fig. 1M, N, P). This observed protection in the *Lyz1*$^{-/-}$ mice was accompanied by elevated Areg and Arg-1 (Fig. 1O, Q, and Fig. S1K), two biomarkers associated with mucosal repair and downstream of the type 2 immune response (Pesce et al., 2009; Zaiss et al., 2006). Thus, *Lyz1* deficiency ameliorated mucosal inflammation during DSS colitis.

Lyz1-deficient intestines had increased population of goblet and tuft cells

We sought to investigate the above observed protective mechanism in the *Lyz1*$^{-/-}$ mice. RNAseq showed increased goblet and tuft cell transcripts and a reduced enterocyte transcriptome (Fig. 2A–C and Fig. S2A). More tuft and goblet cells in *Lyz1*$^{-/-}$ ileum were validated by staining (Fig. 2D–G, Fig. S2B) and increased transcripts of *Klf4* and *Spdef* for goblet cells (Fig. 2H)(Gregorieff et al., 2009; Katz et al., 2002); and *Il25* and *Pou2f3* for tuft cells (Fig. 2I)(Gerbe et al., 2016; von Moltke et al., 2016). A pronounced goblet cell hyperplasia in the *Lyz1*$^{-/-}$ ileum was accompanied by abnormally smaller Paneth cell electron-dense granules surrounded by expanded electron-lucent halos formed by packaging of Muc2 mucin (compare *Lyz1*$^{-/-}$ in Fig. 2K to WT in 2J and Fig. S2C, D) (Stahl et al., 2018).

Tuft cell-derived IL-25 instructs goblet cell differentiation via promoting type 2 cytokine-producing cells in the intestine (Gerbe et al., 2016; Howitt et al., 2016; von Moltke et al.,

2016). RNAseq and qPCR showed elevated *Il25*, *Il13*, *Gata3*, and Il4 (Fig. 2C, I, L, and Fig. S2E), along with an IL-13 signaling gene set (Fig. 2M). However, qPCR did not detect significant changes in cytokines or transcription factors for type 1, type 3, or T-regulatory cells (Fig. S2F–H). Thus, a skewed type 2 immune profile existed in *Lyz1*$^{-/-}$ intestines consistent with an activated goblet and tuft cell program.

The anti-colitogenic protection in the *Lyz1*$^{-/-}$ mice requires IL-13-IL-4Ra-Stat6 axis

IL-13 secreted from ILC2s promotes goblet and tuft cell differentiation (Gerbe et al., 2016; Howitt et al., 2016; von Moltke et al., 2016). *Lyz1*$^{-/-}$ mice treated with neutralizing anti-IL-13 antibody (Proust et al., 2003) had reduced goblet and tuft cells when compared to isotype control-treated *Lyz1*$^{-/-}$ littermates (Fig. 2N, and Fig. S2I). IL-13 signals through *IL-4R*a receptor (Doran et al., 2017; Rael and Lockey, 2011). The epithelial phenotype of *Lyz1*$^{-/-}$; *Il4ra*$^{-/-}$- mice was reversed to that of WT littermates (Fig. 2O, and Fig. S2J). IL-13 drives type 2 immune response via Stat6 (Doran et al., 2017; Rael and Lockey, 2011). We transplanted bone marrow from *Stat6*$^{-/-}$ mice into total body irradiated *Lyz1*$^{-/-}$ recipients (carrying WT *Stat6* in IECs). Chimeras with *Stat6*$^{-/-}$ bone marrow showed a reduction in goblet cells compared to *Lyz1*$^{-/-}$ recipients reconstituted by WT bone marrow (Fig. 2P and Fig. S2K). Thus, the IL-13-IL-4Ra-Stat6 axis was responsible for the epithelial repopulation in *Lyz1*$^{-/-}$ intestines in homeostasis.

Areg and Arg1 are critical components of type 2 immune signaling (Pesce et al., 2009; Zaiss et al., 2006); and both were elevated in the colon of DSS-treated *Lyz1*$^{-/-}$ mice (Fig. 1Q). We examined pStat6 in DSS-treated colons and found a 7-fold increase of this type 2 immune response indicator (Kaplan et al., 1996) in the inflamed colons of *Lyz1*$^{-/-}$ mice compared to WT littermates (p=0.018, Fig. 2Q). Areg promotes barrier function and tissue repair, protecting against DSS colitis (Chen et al., 2018). We reasoned that the observed type 2 immune activation might mediate the anti-colitogenic effects of *Lyz1*-deficiency, similar to helminth therapy of autoimmune disease (Smallwood et al., 2017), and promote mucosal healing (Gause et al., 2013). With an underlying premise that *Il4ra* is indispensable for type 2 immune response (Noben-Trauth et al., 1997), we challenged *Lyz1*$^{-/-}$*;Il4ra*$^{-/-}$ mice with DSS. Compared to *Lyz1*$^{-/-}$ littermates, DSS-treated *Lyz1*$^{-/-}$*;Il4ra*$^{-/-}$ mice exhibited an exacerbated colitis with a complete loss of body weight recovery (Fig. 2R) with worsened colitis score (Fig. 2S). Thus, an enhanced type 2 immune response mediated protection during DSS colitis in *Lyz1*$^{-/-}$ mice.

scRNAseq revealed immune-activated ILC2 in *Lyz1*$^{-/-}$ ileal LP

To define *Lyz1*$^{-/-}$ intestinal immune cell composition, we performed a single cell RNA sequencing (scRNAseq) analysis using ileal LP of separately housed *Lyz1*$^{-/-}$ and WT littermates. Unsupervised separate clustering of WT and *Lyz1*$^{-/-}$ samples identified 23 and 19 clusters, respectively (Fig. S3A). WT ILC2 clusters contained 1,017 cells out of 8,011 total LP cells, while *Lyz1*$^{-/-}$ ILC2 clusters had 844 cells out of 6,733 total LP cells (Fig. 3A). The ILC2 percentage was unchanged (12.7% vs. 12.5%). However, compared to WT LP, *Lyz1*$^{-/-}$ LP displayed a 14.3%, 12.9%, 10.9% and 4.7% increase in *Il1rl1*$^{+}$*Il33r*$^{+}$, *Il5*$^{+}$, *Areg*$^{+}$, and *Il13*$^{+}$ cells, respectively (Fig. 3B).

Combined clustering of all WT and *Lyz1*$^{-/-}$ LP cells revealed 23 clusters (Fig. 3C, D). Clusters 1 and 16 were identified as ILC2s based on signature genes (Fig. 3E, Fig. S3B). Distinct transcriptomic profiles of WT and *Lyz1*$^{-/-}$ ILC2s were evident through heatmap analysis (Fig. 3F, Fig. S3C). Known ILC2 signatures genes (Wallrapp et al., 2017), *Areg*, *Il5*, and *Il1rl1* were highly elevated in *Lyz1*$^{-/-}$ ILC2s (Fig. 3F–I), along with others with documented roles in promoting type 2 immune response, e.g., *Ptgs2* and *Irf4* (Kalinski, 2012; Williams et al., 2013).

WT and *Lyz1*$^{-/-}$ ILC2s could be further partitioned into 9 sub-clusters (Fig. 3J, 3K), with sub-clusters 2 and 8 dominated by *Lyz1*$^{-/-}$ ILC2s (Fig. 3L). The expression of 7 ILC2 signature genes (*Il1rl1*, *Gata3*, *Klrg1*, *Il4*, *Il5*, *Il13*, and *Areg*) was elevated in sub-cluster 2 (Figure. 3M, O, and Fig. S3D), with *Il1rl1* being highly expressed (Figure. 3N, O). ILC2 cells signal through *Il1rl1-Il33r*, and drive Areg production for tissue repair (Herbert et al., 2019; Kabata et al., 2018) (Fig. 3P). Expansion of this subset in *Lyz1*$^{-/-}$ suggested a distinct heterogeneity between WT and *Lyz1*$^{-/-}$ ILC2s. Gene ontology analysis of *Lyz1*$^{-/-}$ versus WT ILC2 revealed significant induction of type 2 immune responses in *Lyz1*$^{-/-}$ mice (Fig. 3Q, Fig. S3E). In contrast to *Lyz1*$^{-/-}$ ILC2s, induction of Th1 cytokine, activation of IFN-γ and reactive oxygen species were revealed in WT ILC2s (Fig. 3Q, Fig. S3F).

Using a dot blot array, we examined cytokines secreted from single cell suspensions of mesenteric lymph nodes (MLNs) isolated from separately housed WT and *Lyz1*$^{-/-}$ littermates in homeostasis (Fig. 3R, Fig. S3G). After 24 hours of *in vitro* culture, *Lyz1*$^{-/-}$ MLNs secreted about 700-fold higher amount of IL-13 compared to WT MLNs (Fig. 3S–U). The secretion of CCL2 (MCP-1) known to control Th2 polarization (Gu et al., 2000) was also increased in *Lyz1*$^{-/-}$ MLNs (Fig. 3S, U). WT MLNs produced more IL-1a and CCL5 than *Lyz1*$^{-/-}$ MLNs (Fig. 3S–U). CXCL-9, CXCL-10, CXCL-13, and IL-2 were below detection limit in *Lyz1*$^{-/-}$ MLNs (Fig. 3S, U and Fig. S3H), consistent with a reduced inflammatory response (Fig. 1L). *Lyz1*$^{-/-}$ MLN cell lysates had elevated pStat6 compared to WT MLN (Fig. 3V and Fig. S3I). Thus, *Lyz1*$^{-/-}$ intestinal mucosa had an activated type 2 immune profile.

Altered mucosal immunity in *Lyz1*$^{-/-}$ mice is microbiota-dependent

We sought to determine the signal upstream of the observed mucosal changes. We noticed that pre-weaning *Lyz1*$^{-/-}$ pups showed no difference of goblet cell composition from their WT littermate (Fig. 4A), suggesting that the mucosal changes occurred in adulthood. Enteroids cultured from WT and *Lyz1*$^{-/-}$ adult mice in regular ENR medium had equivalent goblet and tuft cell numbers or specific transcripts (Fig. 4B–D). When recombinant IL-13 (Huaux et al., 2003) was added, similar goblet and tuft cell differentiation was observed in WT and *Lyz1*$^{-/-}$ enteroids (Fig. 4B–D, Suppl. 4A–B). Thus, the observed goblet and tuft cell phenotype in *Lyz1*$^{-/-}$ mice was not epithelial cell-intrinsic and required non-epithelial signals.

We then treated separately housed WT and *Lyz1*$^{-/-}$ adult littermates with a cocktail of antibiotics (Abx) in drinking water (Rakoff-Nahoum et al., 2004) to test the role of *Lyz1*$^{-/-}$ gut microbiota. Bulk RNAseq showed that Abx-treated *Lyz1*$^{-/-}$ ileum had a reduced type 2 immune signature (Fig. 4E). IL-13 responsive gene set was markedly reduced Abx-treated

mouse ileum (Fig. 4F). Abx treatment also reduced goblet (Fig. 4G) and tuft cell signatures in the *Lyz1*$^{-/-}$ ileum (Fig. 4H). These results were validated by immunostaining and qPCR (Fig. 4I–K, Fig. S4C). Importantly, Abx treatment did not affect NLR signaling in *Lyz1*$^{-/-}$ mice, consistent with a lack of lysozyme-mediated cell-wall processing in *Lyz1*$^{-/-}$ mice (Fig. 4L). When Abx-treated WT and *Lyz1*$^{-/-}$ mice were challenged by DSS (Fig. 4M), a more exacerbated colitis was found in Abx-treated *Lyz1*$^{-/-}$ mice than in those with regular water (Fig. 4N–O). Thus, gut microbiota of *Lyz1*$^{-/-}$ mice was required for the type 2 immune profile and the anti-colitogenic effect.

Lyz1 deficiency changed the gut microbiota landscape

Despite lysozyme's reported bactericidal function, *Lyz1*$^{-/-}$ mice showed no change in luminal bacterial load in cecum or mucosa-associated bacteria in ileum and colon (Fig. 5A). All analyses were performed on littermate WT and *Lyz1*$^{-/-}$ mice from *Lyz1*$^{+/-}$ breeding pairs, and no commercial WT mice were used in our experiments. 16S rRNA amplicon profiling of fecal and ileal content showed unchanged α-diversity between WT and *Lyz1*$^{-/-}$ microbiota (Fig. 5B, Fig. S5A). However, unweighed UniFrac analysis revealed statistically significant difference in fecal (p=3.356E-5, Fig. 5C) and ileal (p=0.014, Fig. S5B) bacterial composition. To determine the cage versus genotype effects, WT and *Lyz1*$^{-/-}$ mice from the same breeding parents were co-housed for 3 weeks, separated into different cages according to genotype (total of 8 WTs in 3 cages; 10 *Lyz1*$^{-/-}$s in 4 cages), and tested after 1-month of separate housing to assess bacterial composition. Principal coordinate analyses (PCoA) of fecal bacterial compositions revealed a significant separation driven by genotype when cage was considered as a random effect in a mixed linear model (Fig. 5D, F) (McCafferty et al., 2013). One-way ANOVA showed that cage effects only contributed to differences among mice of the same genotypes (Fig. 5E, F). PCoA showed a separation of ileal luminal bacteria of separately housed WT and *Lyz1*$^{-/-}$ mice (Fig. 5G). Linear Discriminant Analysis (LDA) for ileal luminal bacteria revealed an expansion of *Ruminococcus gnavus, Blautia gnavus, and Dorea formicigenerans* and a reduction of *Candidatus Arthromitus* (segmented filamentous bacteria) in *Lyz1*$^{-/-}$ mice (Fig. 5H). LDA of fecal bacteria also showed relative expansion of *D. formicigenerans* and reduction of *Candidatus Arthromitus* (Fig. S5C), while LDA of ileal mucosa-associated bacteria identified a reduced abundance of *Candidatus Arthromitus* (Fig. S5D). Thus, *Lyz1* deficiency altered gut bacterial landscape.

Ectopic lysozyme production in colon reduced lysozyme-sensitive bacteria

To obtain detailed insights into how epithelial lysozyme might shape bacterial composition, we developed a second mouse model: *Villin-Lyz1*^{TG} transgenic mice (TG). We used a 12.4 Kb Villin-1 promoter to drive *Lyz1* expression (Fig. 5I), in order to model ectopic lysozyme production seen in human UC (Fig. 1A). Two independent TG founders were validated (Fig. S5E) and were separately maintained on pure C57BL/6 background. TG colony with their WT littermates were maintained separately from the *Lyz1*$^{-/-}$ colony, therefore WT mice were not shared between studies. TG mice showed an epithelial cell specific lysozyme production in colon (Fig. 5J, Fig. S5F–H), and in small intestinal villi (Fig. S5I). Strong lysozyme immunoreactivity in TG mouse colonic lumen echoed a robust lysozyme enzymatic activity (Fig. 5K), providing us the rationale to examine the impact of ectopic

lysozyme on colonic microbial landscape. When challenged by DSS, TG mice exhibited an exacerbated colitis compared to WT littermates (Supp. Fig. 5K–M).

Fecal bacterial 16S rRNA amplicon profiling did not detect a change in α-diversity (Fig. S5J). Unweighed UniFrac analysis showed a strong separation between *WT* and TG microbiota (p=5.736E-6, Fig. 5K). Parallel examination suggested that *Lyz1*$^{-/-}$ mouse fecal microbiota had an expansion in *Firmicutes* and reduction in *Bacteroidetes* compared to their WT counterparts (Fig. 5M), while these phyla in TG mice altered in an opposite direction compared to their WT controls (Fig. 5N).

Thirty-six species showed a relative increase in *Lyz1*$^{-/-}$ feces (Table. S1), and 25 of them belonged to *Firmicutes* phylum represented by *Dorea, Ruminococcus, Robinsoniella, Acetatifactor*, and *Tyzzerella* genera (Fig. S5N). Species were decreased in TG, with 19 belonging to *Firmicutes* (Fig. S5O). Cross-comparison revealed 13 species expanded in *Lyz1*$^{-/-}$ but decreased in TG (Table. S2). Ranking by relative abundances gave rise to top 9 species with >1,000 amplicons detected in at least one genotype (Table. S2, Table. S3). Among them, *R. gnavus, D. formicigenerans*, *M schaedleri*, *A. muciniphila* were also expanded in *Lyz1*$^{-/-}$ ileal luminal microbiota (Fig. S5P, Table. S3, Table. S4). Similar comparison revealed 7 species increased in TG but decreased in *Lyz1*$^{-/-}$ mice, with the top one being *Lactobacillus murinus* (Table. S5). *Candidatus Arthromitus* showed an expansion in TG but a reduction in *Lyz1*$^{-/-}$ mice (Fig. 5H, Table. S5, Fig. S5C–D). LDA independently identified *D formicigenerans* and *L. murinus* as top expanded species in *Lyz1*$^{-/-}$ and TG fecal microbiota, respectively (Fig. S5C and 5Q).

Among the top expanded species in *Lyz1*$^{-/-}$, *R. gnavus, D. formicigenerans, M. schaedleri, and A. muciniphila* were mucolytic bacteria (Png et al., 2010; Tailford et al., 2015b) (Robertson et al., 2005) (Table. S3). Both *D. formicigenerans and R. gnavus* contain genes for sialic acid metabolism and mucin degradation (Tailford et al., 2015a). Expansions of these species were observed in 3 independent 16S rRNA sequencing experiments (Fig. 5O, P).

The reverse alterations of certain species under lysozyme deficiency and overproduction suggested their sensitivities to luminal lysozyme. We thus tested the growth sensitivity to lysozyme for a selective panel of culturable bacteria. In anaerobic condition, *D. formicigenerans* was highly sensitive to lysozyme at the exponential growth phase upon exposure to 20 μg/mL of hen egg lysozyme (Fig. 5Q, Fig. S5R). A separate *Dorea* genus member, *D. longicatena*, showed similar lysozyme sensitivity (Fig. 5R). *R. gnavus* growth in L-YHBHI.4 medium was unchanged when exposed to lysozyme during exponential or lag phases (Fig. S5S). However, when cultured in DP2 defined media (see Methods), the growth of *R. gnavus* was prevented by lysozyme added at the time of or 30 min after inoculation of culture (Fig. 5S). Addition of lysozyme 60 min after inoculation only partially prevented growth of *R. gnavus*. If lysozyme was added 4 hr after inoculation of the culture, the bacteria were largely resistant (Fig. S5T), indicating potential density-dependent resistance similar to collective antibiotics resistance reported previously (Brook, 1989; Tan et al., 2012). When the same time course was conducted for *R. gnavus* cultured in L-YHBHI.4, the lysozyme remained ineffective in suppressing its growth, indicating an environment-dependent

lysozyme sensitivity. *A. muciniphila* was insensitive to lysozyme during any growth phase (Fig. 5T). Likewise, *B. uniformis*, despite expansion in *Lyz1*$^{-/-}$ (Fig. S5C), and *L. rhamnosus* were both resistant to lysozyme (Fig. 5U, V). These distinct growth responses of commensal bacteria to lysozyme indicated drastically different lysozyme-mediated bacterial killing (Ellison and Giehl, 1991; Ibrahim et al., 2001a; Laible and Germaine, 1985).

Microbiota from *Lyz1*$^{-/-}$ mice does not offer anti-colitogenic protection when transferred into "lysozyme-sufficient" recipients

To test if the anti-inflammatory activity of *Lyz1*$^{-/-}$ microbiota could be transferred to recipients with intact Lyz1, we performed fecal microbiota transfer (FMT) using germ-free (GF) C57BL/6 recipients. Bacterial suspensions pooled from the ceca of WT (N=3), *Lyz1*$^{-/-}$ (N=3), or TG (N=3) mice were gavaged to WT GF mice (N=5 for each genotype of FMT, Fig. 6A). 16S rRNA amplicon profiling validated colonization after a week and successful maintenance of distinct WT, *Lyz1*$^{-/-}$, or TG microbiota in individual GF recipients (Fig. 6B). Following FMT of *Lyz1*$^{-/-}$ microbiota, abundance of *Firmicutes* was reduced, while *Bacteroidetes* expanded after a week (Fig. 6C). qPCR showed reduced abundance of *R. gnavus* and *D. formicigenerans* in *Lyz1*$^{-/-}$-FMT recipients 1-week after transfer (Fig. 6D), likely due to the intact host lysozyme activity. Despite this partial reduction, PERMANOVA and ANOSIM analysis (Ericsson et al., 2018), using genotype or duration of colonization as variables, showed that the genotype of FMT donors played the dominant role in defining the observed separation rather than the duration of colonization (Fig. 6E).

To test whether FMT of *Lyz1*$^{-/-}$ or TG microbiota might modulate the response to DSS, GF mice transplanted with WT, *Lyz1*$^{-/-}$, or TG microbiota were treated with regular water or 3% DSS (Fig. 6F). Unexpectedly, *Lyz1*$^{-/-}$-FMT mice exhibited an exacerbated colitis (Fig. 6G, H), loss of 20% of body weight on average (N=5, Fig. 6I), and a 20% mortality at the end of the study. All WT-FMT and TG-FMT mice survived the treatment. TG-FMT mice exhibited a degree of protection judged by histology (Fig. 6G, H) and body weight change ($p>0.05$, Fig. 6I).

NanoString transcriptome analysis using nCounter Inflammation Panel (Mouse v2) of DSS-treated mouse colonic mucosa showed that inflammatory genes were generally elevated in all DSS-treated mice (Fig. S6A–C). Among 13 genes affected exclusively in *Lyz1*$^{-/-}$-FMT mice were elevated inflammatory transcripts: Hif1a, Ptgs2, Csf2, Csf3, and anti-inflammatory Areg, Arg-1, and Cd163 (Fig. 6J). Immunostaining verified Areg elevations in *Lyz1*$^{-/-}$-FMT colons (Fig. 6K, L). pStat6 and pStat3 proteins were also elevated in *Lyz1*$^{-/-}$-FMT, compared to WT-FMT and TG-FMT colons (Fig. 6M–P and Fig. S6D, E). Thus, transferring *Lyz1*$^{-/-}$ microbiota to lysozyme-sufficient recipients exacerbated colitis likely through enhanced bacterial processing by host lysozyme. This increased inflammatory response likely masked Areg's tissue repair activity.

TG-FMT mouse colonic mucosa had reduced inflammatory response compared to WT-FMT or *Lyz1*$^{-/-}$-FMT mice, exhibited by reduced MAPK, NF-κB, T-cell receptor, and natural killer cell cytotoxicity pathways (Fig. S6F). Oas2, Mx1, and cell death-related genes Fasl and Rock2, were among the most reduced transcripts in TG=FMT mice during DSS colitis

(Fig. 6J). Thus, transfer of *Lyz1*$^{-/-}$ microbiota to lysozyme-sufficient hosts did not transfer protection.

Lysozyme-processed and non-processed *R. gnavus* induced different immune responses

We postulated that lysozyme-sensitive bacteria might elicit varying immune responses dependent upon lysozyme processing. We chose *R. gnavus* to test this hypothesis due to its expansion in IBD patients (Hall et al., 2017; Joossens et al., 2011; Sartor and Mazmanian, 2012; Willing et al., 2010). *Lyz1*$^{-/-}$ mice carrying high abundance of *R. gnavus* also showed more goblet cells (Fig. S7A). We tested the impact of live *R. gnavus* and *lysozyme*-processed *R. gnavus* on intestinal MLN cells. Supernatants were collected from live *R. gnavus* or lysozyme-treated *R. gnavus*, applied to WT or *Lyz1*$^{-/-}$ MLN cells, and examined for cytokine production using dot blots (Fig. 7A and Fig. S7B). Supernatants of non-processed *R. gnavus* elicited a 5-fold induction of IL-13, among other cytokines from MLN cells from WT (Fig. 7B, D, E) and *Lyz1*$^{-/-}$ mice (Fig. 7C, D, E). In contrast, lysozyme-processed *R. gnavus* failed to induce IL-13, and instead induced a range of inflammatory cytokines: TNFa, CXCL1, CXCL2, CXCL9, CXCL10, CCL3, IL-6, and IFNγ (Fig. 7B, D, E). Different from lysozyme-processed *R. gnavus*, heat-killed *R. gnavus* induced a confined panel of cytokines from WT and *Lyz1*$^{-/-}$ MLNs (Fig. S7C, D). Lysozyme-treated *L. rhamnosus* (a lysozyme-resistant control, Fig. 5V) was the least effective (Fig. S7E, F), suggesting that the observed cytokine induction was specific to lysozyme-processed *R. gnavus*, and not due to lysozyme alone (Fig. 7D). Live *R. gnavus* supernatants also promoted pStat6, whereas lysozyme-processed *R. gnavus* induced pStat3 (Fig. 7F, Fig. S7G, H) in WT and *Lyz1*$^{-/-}$ MLNs. Thus, live and lysozyme-processed *R. gnavus* elicited different MLN cytokine profile.

To test if *R. gnavus* elicits distinct immune response *in vivo* in *Lyz1*-sufficient versus -deficient hosts, *WT* and *Lyz1*$^{-/-}$ littermates were first treated by Abx, followed by colonization with *R. gnavus* (Fig. 7G), or *L. rhamnosus* (as a lysozyme-resistant control). Successful colonization was confirmed by PCR (Fig. S7I, J). Bulk RNAseq showed that *R. gnavus* colonization of Abx-treated *Lyz1*$^{-/-}$ mice restored the type 2 responses (Fig. 7H–K), which had been diminished by Abx treatment (Fig. 4E, F, H). qPCR validated the increased IL-13 and IL-25 after *R. gnavus* colonization of Abx-treated *Lyz1*$^{-/-}$ mice (Fig. S7K, L). Immunostaining confirmed that *R. gnavus,* but not *L. rhamnosus,* induced expansion of goblet and tuft cells (Fig. S7M–O). Of note, although *R. gnavus* increased goblet and tuft cells in WT mice (Fig. S7M–O), it elicited a more potent type 2 response in *Lyz1*$^{-/-}$ than in WT mice (Fig. S7P).

To assess the modulatory effects of processed and uprocessed *R. gnavus* on experimental colitis, WT and *Lyz1*$^{-/-}$ Abx-treated mice were first colonized with *R. gnavus* and then treated with DSS (Fig. 7L). Abx-treated *Lyz1*$^{-/-}$ mice developed severe colitis (Fig. 4N–O), however, *R. gnavus* colonization ameliorated it (Fig. 7M–O). *R. gnavus* colonization of Abx-treated WT mice exacerbated colitis (Fig. 7M–O). We concluded that host *Lyz1* status balanced the pro- or anti-inflammatory effects of lysozyme-sensitive bacteria.

DISCUSSION

Abnormalities in Paneth cell lysozyme granules and secretory defects were reported in CD patients (Liu et al., 2017; VanDussen et al., 2014) and in mice carrying CD susceptibility alleles (Bel et al., 2017). In UC, metaplastic Paneth cells in left colon are a feature of this disease (Singh et al., 2020; Tanaka et al., 2001). We found that these metaplastic Paneth cells expressed lysozyme. We used *Lyz1*-deficient and -overexpressing mice to model these aberrant lysozyme productions, and revealed that luminal lysozyme abundance controls the composition of ileal and colonic microbiota, regulating mucosal inflammatory responses at steady-state and during experimental colitis.

Prior *in vitro* work suggested that lysozyme displayed bactericidal activity towards Gram-positive and Gram-negative species (Ibrahim, 1998) (Ellison and Giehl, 1991; Ibrahim et al., 2001a; Laible and Germaine, 1985). We found that bacterial load and alpha diversity in multiple anatomical regions were not affected by lysozyme deficiency or overproduction, which was counterintuitive of the notion that lysozyme is non-specific antimicrobial peptide (Ragland and Criss, 2017). Our data suggest that distinct bacterial populations possess differential sensitivity to lysozyme. For example, *Lactobacilli* were resistant to lysozyme, while *Dorea* were very sensitive. Among lysozyme-sensitive species, the growth of *D. formicigenerans* versus *R. gnavus* also exhibited variable responses to lysozyme. Thus, a fine-tuned microbial or host-microbe factors may exist to determine the distinct lysozyme-sensitive profiles of individual commensal species.

A diminished intestinal lysozyme secretion in certain IBD patients may allow a selective expansion of species such as *R. gnavus* (Hall et al., 2017; Joossens et al., 2011; Sartor and Mazmanian, 2012; Willing et al., 2010). Conversely, ectopic production of lysozyme by metaplastic Paneth cells in inflamed UC colons may suppress lysozyme-sensitive species but nevertheless drive inflammation through bacterial cell-wall processing. Such interplay between host lysozyme and microbiota may also exist in $Lyz2^{-/-}$ mice that lack lysozyme M in macrophages and neutrophils. $Lyz2^{-/-}$ mice displayed higher susceptibility to pulmonary infection by *M. luteus or S. pneumonia* (Ganz et al., 2003; Markart et al., 2004b; Shimada et al., 2008). These studies suggested that the exacerbated inflammation in $Lyz2^{-/-}$ mice were due to the failure of lysozyme M to inactivate peptidoglycan. However, $Lyz1^{-/-}$ ileal mucosa had a diminished mucosal sensing and response to bacterial peptidoglycan at steady state, accompanied by reduced basal inflammatory response. Thus, the different sites where these lysozymes are produced may contribute to the observed differences. Monocytic lysozyme M may mediate direct bacterial killing to prevent infection spreading, while luminal lysozyme P, with an intact barrier, may primarily process bacterial cell-wall to alert the immune system.

Lyz1-deficiency led to changes in both epithelial and immune cell compartments. The reshaped gut microbiota in $Lyz1^{-/-}$ mice unexpectedly promoted a type 2 response responsible for goblet and tuft cell expansion. One of the lysozyme-sensitive species, *R. gnavus*, induced a similar type 2 response when colonizing the $Lyz1^{-/-}$ mice, supporting the homeostasis whereby certain commensal bacteria modulate the inflammatory tone as reported in the lungs (Chua et al., 2018). Simultaneous expansion of two phylogenically

related *R. gnavus* and *D. formicigenerans* in *Lyz1*$^{-/-}$ mice may link to their expression of genes for sialic acid metabolism and mucin degradation (Tailford et al., 2015a). Degradation of mucin coupled with the induction of mucin-producing goblet cells by mucolytic bacterial species (Png et al., 2010; Tailford et al., 2015b) may promote syntrophy by fueling the assimilation of mucin monosaccharides by other bacteria (Sartor and Mazmanian, 2012; Willing et al., 2010). *R. gnavus* also promoted goblet and tuft cell program in WT mice, yet it did not exert protection. We speculate that when barrier function is compromised, lysozyme-processed *R. gnavus* may escalate the inflammation that overrides the protective type 2 response. These data collectively support a model whereby the expansion of certain IBD-related species such as *R. gnavus* may promote tissue healing when luminal lysozyme is reduced (Laurent et al., 2017; Pulendran and Artis, 2012).

The exact molecular identities of the bacterial products that skewed the type 2 immune response in *Lyz1*$^{-/-}$ mice are unknown. Live, non-processed *R. gnavus,* or similar bacteria, may generate products eliciting cytokines such as IL-13. Notably, tuft cells sense gut microbial metabolites through taste receptors and GPR91 to promote an ILC2 immune circuit (Howitt et al., 2016; Lei et al., 2018; Nadjsombati et al., 2018; Schneider et al., 2018). Bacterially derived succinate engages GPR91 to initiate type 2 immune response (Lei et al., 2018; Nadjsombati et al., 2018; Schneider et al., 2018). *R. gnavus* may not be a strong succinate producer based on pilot study. Helminths are capable of inducing tuft cell hyperplasia and type 2 response in Gpr91-deficient mice (Nadjsombati et al., 2018), indicating multiple gut biome-initiated pathways promoting differential mucosal immune response.

Based on our analysis, it is reasonable to propose that processing of sensitive bacterial cell walls by lysozyme drives inflammatory response in mucosal immune cells. Elevated lysozyme production during active colitis is expected to enhance bacterial processing and killing, which prevents bacterial infiltration but exacerbating type 1 and 3 inflammation.

A study found that co-culture of intestinal organoids with Th1 cells increased Paneth cell specific genes, while IL-13 treatment increased tuft cell differentiation (Biton et al., 2018) leading to a notion that distinct Th cytokines guide MHCII^{+}Lgr5^{+} stem cells to specific epithelial cell types. Paneth cells possibly monitor and direct the intestinal type 1 immunity via lysozyme while goblet and tuft cells coordinate with type 2 immunity. In so doing, the Th1-Paneth cell axis is balanced by goblet-tuft-Th2 circuit to maintain gut homeostasis.

LIMITATIONS OF STUDY

Currently, no murine model precisely models the lysozyme-producing metaplastic Paneth cells in distal colon of IBD patients. The *Villin-Lyz1* transgenic mice developed in this study were not colon-specific and, as such, lysozyme was overexpressed in epithelia throughout the entire intestinal tract. As the abundance of luminal lysozyme in these mice was expected to be greater than produced solely by metaplastic Paneth cells in human IBD, the experimental colitis exhibited in *Villin-Lyz1* mice should be interpreted with caution. The colitis study used in current study was limited to the well-established DSS model. Additional research will elucidate the role of lysozyme in various inflammatory models, in

particular during pathogen infection. The insights into the impact of other lysozyme-sensitive bacterial species remain limited. Future work will define species-specific impact, under lysozyme-deficient and sufficient conditions, on mucosal inflammatory response. The mechanism of the anti-inflammatory activities of *Villin-Lyz1* mouse gut microbiota, when transferred to gnotobiotic mice, remained unclear. Future work will identify the specific species mediating such protection.

STAR METHODS

Detailed methods are provided in the online version of this paper and include the following:

RESOURCE AVAILABILITY

Lead contact—Further information and requests for reagents should be directed to, and will be fulfilled by, the Lead Contact, Nan Gao at Rutgers University-Newark. email: ngao@newark.rutgers.edu.

Materials availability—Mouse lines generated in this study are available upon request.

Data and code availability—The scRNA-seq data generated in this study are deposited in Gene Expression Omnibus(GEO) with accession number GSE151152. The bulk RNA-seq data generated in this study are deposited in GEO with accession number GSE151151.

EXPERIMENTAL MODEL AND SUBJECT DETAILS

Mice—*Lyz1*$^{-/-}$ mice were derived in a previously published study (Yu et al., 2018) where the *Lyz1* gene was disrupted by a knock-in gene cassette “H2BmCherry-IRES-CreER”. The mouse allele was backcrossed to C57BL/6 for 8 generations. To generate *Villin-Lyz1*^{TG} mice, mouse Lyz1 coding sequence was amplified using ileal tissue cDNA and inserted at *XhoI* and *AgeI* sites of a 12.4kbVillin-ΔATG vector (Addgene, Plasmid #19358), in which a 12.4kb-length Villin promoter directs the Lyz1 expression in intestinal epithelial cells (Madison et al., 2002). The construct was digested with *PmeI* to remove pUC18 vector backbone. The linearized DNA fragment containing Villin promoter/ Lyz1CDS/SV40 polyA signal sequences was separated by 0.8% agrose gel, purified and subjected to DNA dialysis in microinjection buffer (8 mM Tris-HCl, 0.15 mM EDTA). After dialysis, the DNA fragment was diluted to 2ng/μl with microinjection buffer and used for pronuclear microinjection on C57BL/6 genetic background. 6 founders were identified using genotyping PCR. Two founder lines were confirmed and maintained separately on C57BL/6 background. The expression of Lyz1^{TG} was tested on F1 pups by real-time PCR, western blot and immunofluorescence. *Stat6*$^{-/-}$ (Stock No. 005977) and *Il4ra*$^{-/-}$ (Stock No. 003514) mice were purchased from Jackson Laboratory.

All animal experiments were approved and overseen by the Institutional Animal Care and Use Committee of Rutgers University and University of Arizona. Animal experiments were conducted in accordance with NIH guidelines and US federal laws. All mice were housed in individually ventilated cages under specific pathogen free conditions at Rutgers University Newark animal facility or University of Arizona gnotobiotic facility accredited by the Association of Assessment and Accreditation of Laboratory Animal Care International. All

mice were maintained on a 12-hour light/dark cycle and fed by food and water ad libitum. All experiments were performed on littermates, and data were typically reported on the basis of multiple experiments of independent litters. When WT and *Lyz1*$^{-/-}$ mice were separately housed for an experiment, it was reported as separately housed littermates in the text and figure legend. WT mice throughout the study were generated from the same colonies where *Lyz1*$^{-/-}$ or TG mice were produced. No commercial WT mice were used as controls in any experiment.

Human Samples—The human tissue samples were de-identified and procured under approved Institutional Review Board (Princeton Medical Center: BN2239; BN2294).

Bacterial strains—*Akkermansia muciniphila* (DSMZ, DSM-22959), Bacteroides uniformis (DSMZ, DSM-6597), and *Dorea formicigenerans* (DSMZ, DSM-3992) were grown in appropriated L-YHBHI.4 (Liquid Yeast extract Hemin Brain Heart Infusion.4) growth medium. *Dorea longicatena* (DSMZ, DSM-13814) was grown in 104 PYG modified medium. *Ruminococcus gnavus* (in-house INRA-Micalis collection (Dabard et al., 2001) was grown in either L-YHBHI.4 or DP2 growth medium (Table. S6). For bacteria colonization, *R. gnavus* (ATCC, Catalog No. 29149) was cultured in AnaeroGRO Chopped Meat Glucose Broth (Hardy Diagnostics, Catalog No. AG19H). All anaerobic cultures were conducted at 37°C using the Hungate culture method (Hungate, 1950) at Institut Micalis, INRA, France or Dr. Haggblom's lab at Rutgers-New Brunswick. *Lactobacillus rhamnosus GG* (*LGG*, ATCC, Catalog No. 53103) was aerobically cultured in commercial Lactobacilli MRS Broth (BD Biosciences, Catalog No. 288130) in our own lab. For each bacterial specie, 24h growth media were inoculated with a 1:9 dilution to a duplicate set of young culture of similar composition.

METHOD DETAILS

DSS Experimental Colitis—Adult littermates (N=3–14/group) were administered with 3% dextran sulfate sodium (DSS, Colitis grade, 36–50KDa, MP Biologics, SKU 0216011080) in tap water for 7 days and recovered with tap water for another 7 days. Colon tissues were harvested for further pathological analysis. Colonic damage was scored blindly by a GI pathologist as described previously (Chassaing et al., 2014).

Briefly, H&E sections were blindly scored by a certificated pathologist. Scores (0–4) were assigned based on the severity of epithelial injury and leukocyte infiltration into the mucosa, submucosa and muscularis. These three scores were multiplied by an extended factor to assess the extent of the change: 1 for focal, 2 for patchy, and 3 for diffuse, and summed to achieve the final score out of the maximal score of 36. For Figure 6H, colitis score of the dead *Lyz1*$^{-/-}$-FMT mouse was assumed to be equal to the worst colitis score among the *Lyz1*$^{-/-}$-FMT mice.

In vivo IL-13 Neutralization—For IL-13 neutralization, 8–12-week-old mice (N=2 for each genotype in each treatment group) were administrated i.p. with indicated antibody or isotype control at a dose of 250ug/mouse on Day 0 and Day 3. Intestinal tissues were

collected on Day 5 for further analysis. IL-13 neutralizing antibody (Catalog No. MAB413) and Rat IgG2a Isotype control (Catalog No. MAB006) were purchased from R&D systems.

Bone Marrow Transfer—To study the role of lamina propria immune cells in *Lyz1*$^{-/-}$ phenotypes, we derived chimera mice using bone marrow transfer. Briefly, bone marrow from femur and tibias were harvested from gender and age-matched wild type (N=4) and *Stat6*$^{-/-}$ mice (N=4) to generate single cell suspensions (5×10^6 cells/100μl). Recipient mice (WT, N=6; *Lyz1*$^{-/-}$, N=6) received two rounds of whole-body irradiation (6 Gy), 3 hr apart. Then, bone marrow single cells (100 μl) were injected into the irradiated recipients through ophthalmic venous plexus. After 2 mo reconstitution, recipient mice were euthanized, and intestinal tissues were collected for further analysis.

Lysozyme Resistance Assay—To determine whether certain bacterial species were sensitive to lysozyme, 200 μg/L sterile chicken egg white lysozyme solution (Sigma, Catalog No. L6876) was added to each young culture media duplicates at the time of the inoculation of the bacteria into the young culture or during the exceptional phase. The growth of each bacteria was measured every 30min or 1h by absorbance (A660) for 8–10h.

Intestinal Lysozyme Activity Assay—To measure the activity of endogenous lysozyme, we used fluorometric based lysozyme activity assay kit (Abcam, Catalog No. ab211113) according to the manufacturer's instructions. Briefly, luminal contents were centrifuged at 12,000×g for 5 min at 4°C and supernatants were subjected to lysozyme activity assay. 10μl of each supernatant was mixed with 4μl lysozyme substrate in 60μl assay buffer and incubated for 1hr at 37°C. After incubation, 50μl of lysozyme stop buffer was added into each well and subjected to fluorescence measurement (Ex/Em=360/445nm). Serial dilutions of 10μM 4-Methylumbelliferone (4-MU) were used for standard curve preparation. Variation in fluorescence in each sample was applied to the standard curve to get the amount of 4-MU generated during the reaction. The lysozyme activity in the supernatants is calculated as the amount of 4-MU generated in the reaction divided by the reaction time and sample volume.

Antibiotics Treatment and Bacteria Colonization—Age- and gender-matched mice (N=16 for each genotype) were fed with autoclaved tap water containing antibiotics cocktail for one week and recovered on autoclaved tap water without antibiotics for 3 days. Fecal pellets were collected for DNA extraction and real-time PCR using bacterial universal primer set was conducted to ensure bacteria depletion after antibiotics treatment. Then, *R. gnavus* or *LGG* suspension (1×10^8/mouse) in 1.5% $NaHCO_3$ (pH8.0) was gavaged into each mouse (N=10 for *R. gnavus* colonization in each genotype, N=4 for LGG colonization in each genotype). After 1 wk, fecal pellets were collected for *R. gnavus* quantification using real-time PCR with *R. gnavus* specific primer set.

Bacterial DNA Extraction, Sequencing and Analysis—Mouse feces, ileal luminal, or cecum luminal contents were freshly collected and frozen at - 80°C. Genomic DNA was isolated using Qiagen QIAamp DNA Stool Mini Kit (Catalog No. 51604) or Invitrogen PureLink Microbiome DNA purification kit (Catalog No. A29789) according to the manufacturer's instructions. Purified DNA samples were sent to PrimeBio Research Institute

LLC for barcoded 16s rDNA library construction and next-generation sequencing using Invitrogen Ion Torrent Sequencing kit. Briefly, 3 ng of the purified bacteria DNA was used for 16s rRNA PCR amplification. The amplicons were generated with the Ion 16s Metagenomics Kit (Thermofisher, Catalog No. A26216), which amplifies seven hypervariable regions (V2, V3, V4, V6, V7, V8, and V9) of bacterial 16S rRNA. After the 16s rRNA PCR amplification, the Ion Plus Fragment Library Kit (Thermofisher, Catalog No. 4471252) was used for library construction. The constructed libraries were templated with Ion PGM™ Template Hi-Q Kit (Thermofisher, Catalog No. A27739), and then sequenced with Ion PGM™ Hi-Q™ Sequencing Kit (Thermofisher, Catalog No. A25592). The sequencing reads were processed by Ion Torrent Suites and Ion Reporter software Metagenomics 16S w1.1 workflow, which enables the identification, at the genus or species level, of microbes present in complex polybacterial samples via the curated MicroSEQ™ ID 16S rRNA reference database and the curated Greengenes database. In brief, FASTQ quality files were split by samples according to the barcode and BAM files were generated by Ion Torrent Suites. The BAM files were uploaded into Ion Reporter, and reads were filtered by primer and length. Unique reads were kept, and abundance was calculated over a set of thresholds. Taxonomical classification was performed using multistage BLAST search of reads against two databases mentioned above, and OTU tables were created.

Metastats (http://metastats.cbcb.umd.edu/detection.html) was used to detect differentially abundant features between microbial communities of different groups, that is, features that are enriched or depleted in one population versus another. Metastats employs the false discovery rate to improve specificity in high-complexity environments, and separately handles sparsely sampled features using Fisher's exact test. QIIME (qiime.org) was used for microbial ecological Chao1 richness (alpha diversity) and PCoA (beta diversity) assay. Linear Discriminant Analysis (LDA) was performed using LDA Effect size (LEfSe) analysis tool (https://huttenhower.sph.harvard.edu/galaxy/). Briefly, the non-parametric factorial Kruskal-Wallis sum-rank test was used to detect features with significant differential abundance with respect to the species level. Biological significance was subsequently evaluated using a set of pairwise tests among subclasses by unpaired Wilcoxon rank-sum test. Then, LEfSe was applied to estimate the effect size of each differentially abundant feature to perform dimension reduction.

To examine cage effects, WT and *Lyz1*$^{-/-}$ mice from the same breeding parents were co-housed for 3 weeks, separated into different cages according to genotype (e.g. WT cages and *Lyz1*$^{-/-}$ cages), and tested after 1-month of separate housing to assess bacterial composition. Based on a mixed linear model and one-way ANOVA (McCafferty et al., 2013), cage and genotype effects were calculated.

Fecal Microbiota Transplantation and Gnotobiotic Mice—9–10-week old female germ-free C57BL/6J mice maintained in flexible isolators at the University of Arizona gnotobiotic facility were used according to an approved IACUC protocol 07–126 (to P.R.K.). Study was limited to female mice to reduce aggression upon cage transfer and experimental grouping. Fecal microbiota transplantation (FMT) was performed by administering fecal slurry prepared from pooled stools from either WT (N=9), *Lyz1*$^{-/-}$ (N=9) or *Villin-Lyz1*^{TG} (N=10) mice by oral gavage with 100mL of suspension and by painting the abdominal pelt

with the same amount (Day 0). Upon colonization, mice were randomly assigned to control or DSS group (N=5) and transferred to Tecniplast iso-positive ventilated cages (one FMT group/treatment/cage). Mice were allowed to acclimate to the new environment for 7 days (Day 7), after which control mice were continued on autoclaved water, while DSS group received 3% DSS in drinking water for another 7 days (till day 14). Body weight was monitored daily. Mice were euthanized on day 14 and colons were harvested for RNA isolation or fixed in buffered formalin for histological analysis.

Fecal samples from all ex-GF mice were collected at day 0 (the colonization day, serve as a negative control), and then at day 7, and day 14. Fecal pellets were stored at −80°C until use. Genomic DNA was extracted and purified with PowerFecal Pro DNA kit (Qiagen, Cat No. 51804) according to the manual provided by the manufacturer. The samples were homogenized using provided lysis buffer and the tubes pre-filled with the 96 well plate shaker (Mo-Bio, Cat No. 11996) with the 2 ml adapters (Mo-Bio, Cat No 11990) two times 10 minutes at speed 30Hz each at 4°C. The hypervariable V4 region of the 16S rRNA gene was amplified by PCR from each sample using barcoded primers (515F and 806R). The forward primer is common for all samples, whereas the reverse primers, consisting of Golay barcodes, were unique for each sample. Both reverse and forward primes are extended with the sequencing primer pads, linkers, and Illumina adapters (Caporaso et al., 2012). The PCR was performed on LightCycler 96 (Roche) with MyFiTM Mix (Bioline Meridian, Cat No. BIO-25050) in the final volume 40μL. Amplicons were quantified using Quant-It PicoGreen dsDNA Assay kit (ThermoFisher Scientific, Cat No. P7589), according to the manufacturer's protocol. Equal amount of amplified DNA (240ng) from each sample were pooled and cleaned using UltraClean PCR Clean-Up Kit (MoBio, Cat No. 12500). Pooled amplicons were diluted, denatured with NaOH at final concentration 0.1N, and 6.75 pmols of the pooled library was sequenced at our laboratory on MiSeq platform (Illumina) using custom primers (Caporaso et al., 2012). Due to the limited sequence diversity among 16S rRNA amplicons, 5% of the PhiX Sequencing Control V3 (Illumina, Cat No. FC-110–3001) made from phiX174, was added to the run. The pooled 16S rRNA library was subjected to the paired-end sequencing using 2 × 150bp MiSeq Reagent Kit V2 (Illumina, Cat No. MS-102–2002).

De-multiplexing was done using idemp script (https://github.com/yhwu/idemp). Filtering, dereplication, sample inference, chimera identification, and merging of paired-end reads was done with a reference-free Divisive Amplicon Denoising Algorithm 2 (Dada2) R package (Callahan et al., 2017). The ASVs taxonomy was assigned using RDP classifier against SILVA database (Quast et al., 2013) release 132 (https://www.arb-silva.de/documentation/release-132/). The vegan package (https://CRAN.R-project.org/package=vegan) was used as a tool for diversity analysis, ordination methods, for the analysis of dissimilarities, and statistical analysis (Oksanen et al., 2019). The obtained results were visualized with ggplot2 package (Hadley).

Tissue Collection, Fixation and Histochemistry—Mouse intestinal tissues were collected and fixed in 4% paraformaldehyde or 10% neutral formalin overnight. Then tissues were transferred into 70% ethanol and subjected to paraffin embedding at the Histology Core Facility at Rutgers University Hospital Cancer Center. 5μm sections were sliced from

paraffin blocks, rehydrated and subjected to H & E staining. To highlight mucin-producing goblet cells, rehydrated sections were subjected to Alcian blue staining. Alcian blue solution (pH2.5) was applied onto slides and incubated for 30 min at room temperature. Then, slides were washed in running water for 2 min and counterstained with Vector Nuclear Fast Red (Vector Labs, Catalog No. H-3403) for 2 min. Slides were rinsed in running water for 5 min and then subjected to dehydration and mounting with Cytoseal-60 (ThermoFisher Scientific, Catalog No. 8310–4). Images were collected by Nikon TE2000D with NIS Elements D version 4.4 and analyzed by ImageJ software.

Transmission Electron Microscopy—The procedure for transmission electron microscopy was described previously (Gao and Kaestner, 2010; Yu et al., 2014). Briefly, 1–2mm ileal tissues were harvested from age-and gender-matched mice (N=3 for each genotype) and immediately immersed in 0.1M sodium cacodylate containing 2% glutaraldehyde (EM grade) and 2% paraformaldehyde for overnight fixation at cold room. Next day, samples were washed twice with 0.1M sodium cacodylate, then post fixed with 1% buffered OsO4 and stained *en bloc* with 0.1% uranyl acetate. The samples were subjected to dehydration using increasing concentrations of ethanol and then in propylene oxide. After balanced in EMBed-812/propylene oxide (1:1) and 100% EMBed-812, the samples were subjected to embedding using EMBed-812 kit (Electron Microscopy Sciences, Catalog No.14120).

Immunofluorescence and Immunohistochemistry—The procedures for immunofluorescence and immunohistochemistry have been previously described (Yu et al., 2018). Briefly, 5μm paraffin embedded sections were subjected to rehydration and antigen retrieval. Slides were doused into the sub-boiling antigen retrieval buffer (1μM citric acid, pH 6.0 or 1μM EDTA, pH8.0) for 20 min and then immediately transferred into running water. To block endogenous peroxidase activity, slides were incubated in 3% H_2O_2 solution diluted in methanol for 10 min. Then, slides were blocked with PBS buffer containing 0.1% Triton X-100, 2%BSA and 2% normal donkey serum for 2hr at room temperature, and then probed with indicated antibodies at 4°C overnight. Next day, slides were washed with PBS and incubated with either fluorescent dye-conjugated secondary antibodies (immunofluorescence) or Polymer HPR-conjugated secondary antibodies (immunohistochemistry).

For Immunofluorescence, slides were incubated with indicated secondary antibodies for 1 hr at room temperature and then followed by DAPI or Topro3 nuclear counterstaining. Then slides were washed with PBS, air-dried and mounted with Prolong Gold Antifade Mountant (Invitrogen, Catalog No. P36930). Images were collected using Zeiss LSM510 with 40x oil lens and analyzed by ImageJ software.

For Immunohistochemistry, ImmPRESS HRP anti-rabbit or anti-mouse IgG polymer (Vector Labs, Catalog No. MP-7401 and MP-7402 respectively) were used. After 1 hr incubation, slides were washed with PBS and subjected to DAB development. Hematoxylin QS (Vector Labs, Catalog No. H-3404) was used for nuclear counterstaining. Then, slides were dehydrated and mounted with Cytoseal-60.

Mesenteric Lymph Nodes Isolation and Cytokine Detection—Mesenteric lymph nodes (MLNs) adjacent to ileum and colon were collected and meshed against 70μm cell strainer. Single cell suspensions were centrifuged, counted and seeded into 6-well plate at 3×10^6/well density. The MLN cells were cultured in RPMI1640 containing 10%FBS, 2 mM l-glutamine, 1xpenicillin/streptomycin solution, 20 mM HEPES, MEM nonessential amino acids, 1 mM sodium pyruvate and β-mercaptoethanol. The indicated supernatants and lysozyme lysis buffer were added into each well (1:50 v/v). After 24 hr coincubation, cytokines in culture media were detected using commercially available cytokine array kit (R &D systems, Catalog No. ARY006) according to the manufacturer's instructions. All the experiments were performed under the same conditions to reduce the variabilities. Quantification of each cytokine from two duplicate dots were conducted using ImageJ. The MLN cells were harvested in 2x SDS buffer containing 1x Proteinase Inhibitor cocktail (Roche, Catalog No. 5892791001) and 1x Phosphatase Inhibitor cocktail (Roche, Catalog No. 4906845001), denatured under 95°C for 15 min and subjected to western blot analysis.

Intestinal Crypts Isolation and In Vitro Culture—The procedure for Intestinal crypts isolation and in vitro culture was conducted as previously described (Yu et al., 2014; Yu et al., 2018). Briefly, mouse ileal fragments were harvested, washed in PBS and incubated in PBS containing 5mM EDTA for 40 min. After vigorous vortexing, crypt suspensions were passed through 70μm cell strainer and centrifuged at 200×g for 5 min at 4°C. Then, intestinal crypts were counted, and resuspended in Matrigel (Corning, Catalog No. 354230). After Matrigel polymerization, IntestiCult organoid growth media (StemCell Technologies, Catalog No. 06005) was added to each well After 3-day culture, recombinant mouse IL-13 (R&D systems, Catalog No. 413-ML) was added or not and incubated for 2 more days. Then, intestinal organoids were subjected to fixation by 4% paraformaldehyde followed by immunofluorescence.

RNA Extraction, Reverse transcription and Real-time PCR—Tissue RNA isolation was conducted using RNeasy Mini Kit (Qiagen, Catalog No. 74104) according to the manufacturer's instructions. Then 1μg of RNA were subjected to reverse transcription using Maxima First Strand cDNA Synthesis Kit for RT-qPCR (ThermoFisher, Catalog No. K1641). Real-time PCR was performed as previously described with indicated primer sets listed in Table. S7.

Bulk RNA-Seq Analysis—Mouse Ileum fragments (3–4 mice/genotype/treatment) were collected and subjected to RNA extraction. RNA samples were submitted for sequencing using BGISEQ500 (BGI-US). Sequenced files were aligned to mm9 genome index using Kallisto (v0.45.0) (Bray et al., 2016) with default settings and 1000 bootstraps. Reads were normalized in DESeq2 (Build 3.9) using default settings in R. RNA-seq data are deposited in GEO (accession # under being processed). For Gene set enrichment analysis (GSEA) (Subramanian et al., 2005) performed on goblet cell gene signatures (Haber et al., 2017), Tuft signature genes (Nadjsombati et al., 2018), Paneth cell signature genes, and ILC2/Th2 cell signature genes (Robinette et al., 2015), pre-ranked files of differentially expressed genes were calculated by the rank metric = -log(p-value)* SIGN(logFC) (Jia et al., 2015). Heatmap of select goblet cell and Tuft cell genes was generated to visualize fpkms of

individual wildtype and *Lyz1*$^{-/-}$ replicates. For GSEA performed on cytoplasmic pattern recognition receptor (PRR) signaling, NOD-like receptor (NLR) signaling, apoptosis, cytokine production in inflammatory response, and response to IL-13, corresponding molecular signature databases were used to determine significance of differential expression between conditions. One thousand permutations were performed for each gene list tested, normalized enrichment scores (NES) and nominal P values are reported for genes signatures. Heatmaps generated by GSEA are on a relative min max scale. Nominal p-value < 0.05 was considered to indicate significant enrichment.

Single cell dissociation and sorting—The distal ileum of adult WT and *Lyz1*$^{-/-}$ mice (separately housed) were dissected and briefly rinsed in ice-cold PBS (Fisher Scientific, SH30256LS). The tissue was opened longitudinally, rinsed in ice-cold PBS, and further sliced to 1–2 mm pieces. The pieces were rinsed in 30mL of ice-cold PBS by inverting the falcon tube 10–15 times. The pieces were then transferred into fresh 30ml of ice-cold PBS. This step was repeated until the solution remained clear after inverting. Each piece was then transferred to 30 mL crypt isolation buffer, containing 5 mM EDTA (Invitrogen, Catalog No.AM9260G), 2% BSA (Sigma, Catalog No.A3294), and HBSS Ca/Mg-free (Sigma, Catalog No.H9394), and allowed to shake at 37°C for 15 minutes. The tubes were subsequently vigorously shaken to release the epithelial layer from the pieces after which the solution was discarded. This was repeated in another 30ml of crypt isolation buffer. The pieces were then incubated in DMEM/F12 medium (ThermoFisher, 12634–010) for 10 minutes on a petri dish, at room temperature. The solution was discarded, and the pieces were thoroughly minced. 10ml of Hank's balanced salt solution with calcium and magnesium (Sigma, Catalog No.55037C) containing 100 U/mL Collagenase II (ThermoFisher, Catalog No.17101015), 500 U/mL DNase I (Sigma, Catalog No.DN25), was added to the minced tissue and allowed to shake at 37°C for 30 minutes. When tissues completely digested, the solution was passed through a 70μM cell strainer into a 50mL falcon tube. The tubes were centrifuged at 200g for 10 minutes. The pellets were resuspended in 1mL of FACS solution (2% BSA in PBS). The single-cell suspensions were stained with DAPI and immediately subjected to sorting by BD Biosciences Aria II Flow Cytometer (BD FACSAria II). Single viable lamina propria lymphocytes and mesenchymal cells were gated by forward scatter, side scatter and by negative staining for DAPI.

Droplet-based Single Cell RNA-Seq—Cell number and viability were determined by a Propidium Iodide based fluorescence assay using Moxi GO II System, Orflo Prod#MXG102 (ORFLO Technologies, LLC). Droplet-based single-cell partitioning and single-cell RNA-Seq libraries were generated using the Chromium Single-Cell 3′ Reagent v3 Kit (10X Genomics, Pleasanton, CA) on the 10X Chromium Controller as per the manufacturer's protocol. Live cells in single cell suspension with 95% viability were mixed with Gel beads, RT reagents and Partitioning Oil into a Single-Cell 3′ Chip and loaded onto 10X Chromium Controller for GEM generation. Briefly, the protocol includes RT, cleanup, cDNA amplification, fragmentation, end repair & A-tail prep, adapter ligation and incorporation of sample indices into finished libraries, which are compatible with Illumina next-generation sequencing platforms. Sample quantification and quality control were determined using Qubit Fluorometer (Invitrogen, Life Technologies) and TapeStation (Agilent Technologies,

Santa Clara CA) respectively. cDNA libraries were sequenced on Illumina NovaSeq 6000 sequencer (Illumina, San Diego, CA) with a configuration of 28/8/0/91-bp for cell barcode, sample barcode and mRNA reads respectively as recommendation by 10X Genomics. The Chromium Single Cell Software is used to analyze and visualize single cell 3' RNA-seq data produced by the 10X Chromium Platform. The 10X chromium software package includes Cell Ranger Pipelines and Loupe Cell Browser. Cell Ranger pipelines use raw 10X single cell sequencing data from an Illumina sequencer and perform demultiplexing, unique barcode processing, and single cell 3' gene counting. The WT and *Lyz1*$^{-/-}$ count matrix files generated by Cell Ranger were imported to Partek flow software for secondary data analysis. The single cell analysis for this paper was generated using Partek® Flow®, version 9.0, build 9.0.20.0202. Copyright ©; 2020 Partek Inc., St. Louis, MO, USA. For each cell, quality control metrics such as number of read counts, number of detected genes, and percentage of mitochondrial reads were calculated and used to filter out low quality cells. The data was then log2+1 normalized based on counts per million and the genes that were not expressed in at least 99% of the cells were excluded from the data set. For figures 3A–C and 3E–J, the WT and *Lyz1*$^{-/-}$ datasets were analyzed separately. For figures 3K– L, and Suppl. Fig 3A–D, the data was first scaled to remove batch effect, then the merged dataset was used for further analyses. Principal components (PCs) were calculated for the samples and the scree plot was used to determine the number of PCs to be used. Based on the PC value, cells were divided into clusters in an unsupervised fashion. The ANOVA test was used to identify differentially expressed genes (DEGs) for each cluster by comparing genes in all the clusters, filtering genes that were increased by 1.5-fold, and then sorting them by ascending p-value. The clusters were then visualized using t-Distributed Stochastic Neighbor Embedding (t-SNE). Based on previous literature, a list of the genes indicated in figure 3B was curated and used to identify ILC2 populations to study the differences in type 2 response between the WT and *Lyz1*$^{-/-}$ mice. The ILC2 population in WT and *Lyz1*$^{-/-}$ was lasso selected and classified. DEGs were identified for the sub clusters in ILC2 population for each genotype and the signature DEG genes (FDR set up ≤1e-8, fold change>2) were visualized by generating a heat map. Then, trajectory analysis using Monocle 2 was performed on these ILC2 cells. DEGs were identified for each of the states by running gene specific analysis in Partek.

nCounter Analysis of Gene Expression—Colonic mucosal RNA and DNA was isolated using AllPrep DNA/RNA Mini Kit (Qiagen, Catalog No. 80204) using the protocol previously described (Harrison et al., 2018). The protocol was slightly modified to include a bead-beating step. Expression of inflammation-related genes was assessed using nCounter Inflammation Panel (Mouse v2) codecs, nCounter Master Kit (NanoString Technologies, Seattle, WA), and the NanoString nCounter® Analysis System at the University of Arizona Genetics Core facility. Data were analyzed using nSolver Analysis software v4.0 with the nCounter Advanced Analysis module v. 2.0.115 (NanoString Technologies).

Quantification and Statistical Analyses—All graphic data and statistical analyses were conducted using Graphpad Prism (https://www.graphpad.com) and Microsoft Excel Office 365. The data were reported as mean ± SEM in bar graphs. Statistical comparisons between two groups were undertaken using unpaired two-tailed Student's t test. *p*-value was

indicated in corresponding graphs. The immunofluorescent data were reported from 3 to 5 sections of each animal; 2 to 16 mice were used in each experiment unless stated differently. The significant level of enrichment score in the GSEA was computed by an empirical phenotype-based permutation test conducted to reserve the complex correlation structure of gene expression patterns. The phenotype labels were permuted and then the enrichment score of the gene set were recalculated for the permuted data, thus resulting in a null distribution for the enrichment score. The nominal p value of the resulting enrichment score was empirically computed relative to this null distribution as previously described (Subramanian et al., 2005).

Supplementary Material

Refer to Web version on PubMed Central for supplementary material.

ACKNOWLEDGEMENTS

The authors are indebted to Ivaylo I. Ivanov (Columbia University) and Mi-Na Kweon (University of Ulsan College of Medicine) for helpful discussion. We thank Peter Romanienko and Ghassan Yehia (Rutgers Cancer Institute of New Jersey Genome Editing Shared Resource P30CA072720-5922) for deriving *Lyz1*$^{-/-}$ and *Villin-Lyz1* mice, Luke Fritzk (Digital Imaging and Histology Core) for histology, Sukhwinder Singh and Tammy Mui- Galenkamp (Flow Cytometry and Immunology Core) for FACS analysis, Seema Husain (The Genomics Center) for scRNA sequencing, and the excellent technical support from PrimBio Research Institute (Exton, PA). This work was supported by NIH grants (DK102934, DK119198, AT010243, CA178599), NSF/BIO/IDBR grants (1353890, 1952823), ACS Scholar Award (RSG-15-060-01-TBE), Rutgers IMRT award to N.G.; Rutgers Chancellor's SEED grant (to E.M.B.); NIH grant R01CA190558 (to M.P.V.); R01AI134040 (to G.S.Y.); 5R01DK109711, PANDA Endowment in Autoimmune Diseases (to P.R.K.); NSF grants (IOS-1456673, IOS-1754783 to R.P.F.); NIH F31 DK121428 (to S. B.); NJCCR fellowship DCHS19PPC038 (to J. F.); and a CCFA Career Development Award 406794 (to S.Y.).

REFERENCES

Afgan E, Baker D, Batut B, van den Beek M, Bouvier D, Cech M, Chilton J, Clements D, Coraor N, Gruning BA, et al. (2018). The Galaxy platform for accessible, reproducible and collaborative biomedical analyses: 2018 update. Nucleic Acids Res 46, W537–W544. [PubMed: 29790989]

Ashburner M, Ball CA, Blake JA, Botstein D, Butler H, Cherry JM, Davis AP, Dolinski K, Dwight SS, Eppig JT, et al. (2000). Gene ontology: tool for the unification of biology. The Gene Ontology Consortium. Nat Genet 25, 25–29. [PubMed: 10802651]

Balasubramanian I, and Gao N (2017). From sensing to shaping microbiota: insights into the role of NOD2 in intestinal homeostasis and progression of Crohn's disease. Am J Physiol Gastrointest Liver Physiol 313, G7–G13. [PubMed: 28450278]

Bel S, Pendse M, Wang Y, Li Y, Ruhn KA, Hassell B, Leal T, Winter SE, Xavier RJ, and Hooper LV (2017). Paneth cells secrete lysozyme via secretory autophagy during bacterial infection of the intestine. Science 357, 1047–1052. [PubMed: 28751470]

Biton M, Haber AL, Rogel N, Burgin G, Beyaz S, Schnell A, Ashenberg O, Su CW, Smillie C, Shekhar K, et al. (2018). T Helper Cell Cytokines Modulate Intestinal Stem Cell Renewal and Differentiation. Cell 175, 1307–1320 e1322. [PubMed: 30392957]

Bray NL, Pimentel H, Melsted P, and Pachter L (2016). Near-optimal probabilistic RNA-seq quantification. Nat Biotechnol 34, 525–527. [PubMed: 27043002]

Brook I (1989). Inoculum effect. Rev Infect Dis 11, 361–368. [PubMed: 2664999]

Butler A, Hoffman P, Smibert P, Papalexi E, and Satija R (2018). Integrating single-cell transcriptomic data across different conditions, technologies, and species. Nat Biotechnol 36, 411–420. [PubMed: 29608179]

Cadwell K, Liu JY, Brown SL, Miyoshi H, Loh J, Lennerz JK, Kishi C, Kc W, Carrero JA, Hunt S, et al. (2008). A key role for autophagy and the autophagy gene Atg16l1 in mouse and human intestinal Paneth cells. Nature 456, 259–263. [PubMed: 18849966]

Callahan BJ, McMurdie PJ, and Holmes SP (2017). Exact sequence variants should replace operational taxonomic units in marker-gene data analysis. ISME J 11, 2639–2643. [PubMed: 28731476]

Canfield RE, and Liu AK (1965). THE DISULFIDE BONDS OF EGG WHITE LYSOZYME (MURAMIDASE). J Biol Chem 240, 1997–2002. [PubMed: 14301784]

Caporaso JG, Lauber CL, Walters WA, Berg-Lyons D, Huntley J, Fierer N, Owens SM, Betley J, Fraser L, Bauer M, et al. (2012). Ultra-high-throughput microbial community analysis on the Illumina HiSeq and MiSeq platforms. ISME J 6, 1621–1624. [PubMed: 22402401]

Chassaing B, Aitken JD, Malleshappa M, and Vijay-Kumar M (2014). Dextran sulfate sodium (DSS)-induced colitis in mice. Curr Protoc Immunol 104, Unit 15 25.

Chen F, Yang W, Huang X, Cao AT, Bilotta AJ, Xiao Y, Sun M, Chen L, Ma C, Liu X, et al. (2018). Neutrophils Promote Amphiregulin Production in Intestinal Epithelial Cells through TGF-beta and Contribute to Intestinal Homeostasis. Journal of immunology 201, 2492–2501.

Chua HH, Chou HC, Tung YL, Chiang BL, Liao CC, Liu HH, and Ni YH (2018). Intestinal Dysbiosis Featuring Abundance of Ruminococcus gnavus Associates With Allergic Diseases in Infants. Gastroenterology 154, 154–167. [PubMed: 28912020]

Dabard J, Bridonneau C, Phillipe C, Anglade P, Molle D, Nardi M, Ladire M, Girardin H, Marcille F, Gomez A, et al. (2001). Ruminococcin A, a new lantibiotic produced by a Ruminococcus gnavus strain isolated from human feces. Appl Environ Microbiol 67, 4111–4118. [PubMed: 11526013]

Di Ruscio M, Vernia F, Ciccone A, Frieri G, and Latella G (2017). Surrogate Fecal Biomarkers in Inflammatory Bowel Disease: Rivals or Complementary Tools of Fecal Calprotectin? Inflammatory bowel diseases 24, 78–92. [PubMed: 29272479]

Doran E, Cai F, Holweg CTJ, Wong K, Brumm J, and Arron JR (2017). Interleukin-13 in Asthma and Other Eosinophilic Disorders. Front Med (Lausanne) 4, 139. [PubMed: 29034234]

Ellison RT 3rd, and Giehl TJ (1991). Killing of gram-negative bacteria by lactoferrin and lysozyme. J Clin Invest 88, 1080–1091. [PubMed: 1918365]

Ericsson AC, Gagliardi J, Bouhan D, Spollen WG, Givan SA, and Franklin CL (2018). The influence of caging, bedding, and diet on the composition of the microbiota in different regions of the mouse gut. Sci Rep 8, 4065. [PubMed: 29511208]

Fahlgren A, Hammarstrom S, Danielsson A, and Hammarstrom ML (2003). Increased expression of antimicrobial peptides and lysozyme in colonic epithelial cells of patients with ulcerative colitis. Clin Exp Immunol 131, 90–101. [PubMed: 12519391]

Ganz T, Gabayan V, Liao HI, Liu L, Oren A, Graf T, and Cole AM (2003). Increased inflammation in lysozyme M-deficient mice in response to Micrococcus luteus and its peptidoglycan. Blood 101, 2388–2392. [PubMed: 12411294]

Gao N, and Kaestner KH (2010). Cdx2 regulates endo-lysosomal function and epithelial cell polarity. Genes Dev 24, 1295–1305. [PubMed: 20551175]

Gause WC, Wynn TA, and Allen JE (2013). Type 2 immunity and wound healing: evolutionary refinement of adaptive immunity by helminths. Nat Rev Immunol 13, 607–614. [PubMed: 23827958]

Gerbe F, Sidot E, Smyth DJ, Ohmoto M, Matsumoto I, Dardalhon V, Cesses P, Garnier L, Pouzolles M, Brulin B, et al. (2016). Intestinal epithelial tuft cells initiate type 2 mucosal immunity to helminth parasites. Nature 529, 226–230. [PubMed: 26762460]

Girnius S, Skinner M, Spencer B, Prokaeva T, Bartholomew C, O'Hara C, Seldin DC, and Connors LH (2012). A new lysozyme tyr54asn mutation causing amyloidosis in a family of Swedish ancestry with gastrointestinal symptoms. Amyloid 19, 182–185. [PubMed: 22978355]

Gregorieff A, Stange DE, Kujala P, Begthel H, van den Born M, Korving J, Peters PJ, and Clevers H (2009). The ets-domain transcription factor Spdef promotes maturation of goblet and paneth cells in the intestinal epithelium. Gastroenterology 137, 1333–1345 e1331–1333. [PubMed: 19549527]

Gu L, Tseng S, Horner RM, Tam C, Loda M, and Rollins BJ (2000). Control of TH2 polarization by the chemokine monocyte chemoattractant protein-1. Nature 404, 407–411. [PubMed: 10746730]

Haber AL, Biton M, Rogel N, Herbst RH, Shekhar K, Smillie C, Burgin G, Delorey TM, Howitt MR, Katz Y, et al. (2017). A single-cell survey of the small intestinal epithelium. Nature 551, 333–339. [PubMed: 29144463]

Hadley W Ggplot2 : elegrant graphics for data analysis, Second edition. edn.

Hall AB, Yassour M, Sauk J, Garner A, Jiang X, Arthur T, Lagoudas GK, Vatanen T, Fornelos N, Wilson R, et al. (2017). A novel Ruminococcus gnavus clade enriched in inflammatory bowel disease patients. Genome Med 9, 103. [PubMed: 29183332]

Harrison CA, Laubitz D, Ohland CL, Midura-Kiela MT, Patil K, Besselsen DG, Jamwal DR, Jobin C, Ghishan FK, and Kiela PR (2018). Microbial dysbiosis associated with impaired intestinal Na(+)/H(+) exchange accelerates and exacerbates colitis in ex-germ free mice. Mucosal Immunol 11, 1329–1341. [PubMed: 29875400]

Herbert DR, Douglas B, and Zullo K (2019). Group 2 Innate Lymphoid Cells (ILC2): Type 2 Immunity and Helminth Immunity. Int J Mol Sci 20.

Howitt MR, Lavoie S, Michaud M, Blum AM, Tran SV, Weinstock JV, Gallini CA, Redding K, Margolskee RF, Osborne LC, et al. (2016). Tuft cells, taste-chemosensory cells, orchestrate parasite type 2 immunity in the gut. Science 351, 1329–1333. [PubMed: 26847546]

Huaux F, Liu T, McGarry B, Ullenbruch M, and Phan SH (2003). Dual roles of IL-4 in lung injury and fibrosis. J Immunol 170, 2083–2092. [PubMed: 12574379]

Hungate RE (1950). The anaerobic mesophilic cellulolytic bacteria. Bacteriological reviews 14, 1–49. [PubMed: 15420122]

Ibrahim HR (1998). On the novel catalytically-independent antimicrobial function of hen egg-white lysozyme: a conformation-dependent activity. Nahrung 42, 187–193. [PubMed: 9739565]

Ibrahim HR, Matsuzaki T, and Aoki T (2001a). Genetic evidence that antibacterial activity of lysozyme is independent of its catalytic function. FEBS letters 506, 27–32. [PubMed: 11591365]

Ibrahim HR, Thomas U, and Pellegrini A (2001b). A helix-loop-helix peptide at the upper lip of the active site cleft of lysozyme confers potent antimicrobial activity with membrane permeabilization action. J Biol Chem 276, 43767–43774. [PubMed: 11560930]

Jia Z, Zhang X, Guan N, Bo X, Barnes MR, and Luo Z (2015). Gene Ranking of RNASeq Data via Discriminant Non-Negative Matrix Factorization. PLoS One 10, e0137782. [PubMed: 26348772]

Jean E, Ebbo M, Valleix S, Benarous L, Heyries L, Grados A, Bernit E, Grateau G, Papo T, Granel B, et al. (2014). A new family with hereditary lysozyme amyloidosis with gastritis and inflammatory bowel disease as prevailing symptoms. BMC Gastroenterol 14, 159. [PubMed: 25217048]

Joossens M, Huys G, Cnockaert M, De Preter V, Verbeke K, Rutgeerts P, Vandamme P, and Vermeire S (2011). Dysbiosis of the faecal microbiota in patients with Crohn's disease and their unaffected relatives. Gut 60, 631–637. [PubMed: 21209126]

Jostins L, Ripke S, Weersma RK, Duerr RH, McGovern DP, Hui KY, Lee JC, Schumm LP, Sharma Y, Anderson CA, et al. (2012). Host-microbe interactions have shaped the genetic architecture of inflammatory bowel disease. Nature 491, 119–124. [PubMed: 23128233]

Kabata H, Moro K, and Koyasu S (2018). The group 2 innate lymphoid cell (ILC2) regulatory network and its underlying mechanisms. Immunological reviews 286, 37–52. [PubMed: 30294963]

Kalinski P (2012). Regulation of immune responses by prostaglandin E2. J Immunol 188, 21–28. [PubMed: 22187483]

Kaplan MH, Schindler U, Smiley ST, and Grusby MJ (1996). Stat6 is required for mediating responses to IL-4 and for development of Th2 cells. Immunity 4, 313–319. [PubMed: 8624821]

Katz JP, Perreault N, Goldstein BG, Lee CS, Labosky PA, Yang VW, and Kaestner KH (2002). The zinc-finger transcription factor Klf4 is required for terminal differentiation of goblet cells in the colon. Development 129, 2619–2628. [PubMed: 12015290]

Klass HJ, and Neale G (1978). Serum and faecal lysozyme in inflammatory bowel disease. Gut 19, 233–239. [PubMed: 631644]

Kurakawa T, Ogata K, Matsuda K, Tsuji H, Kubota H, Takada T, Kado Y, Asahara T, Takahashi T, and Nomoto K (2015). Diversity of Intestinal Clostridium coccoides Group in the Japanese Population, as Demonstrated by Reverse Transcription-Quantitative PCR. PLoS One 10, e0126226. [PubMed: 26000453]

Laible NJ, and Germaine GR (1985). Bactericidal activity of human lysozyme, muramidase-inactive lysozyme, and cationic polypeptides against Streptococcus sanguis and Streptococcus faecalis: inhibition by chitin oligosaccharides. Infect Immun 48, 720–728. [PubMed: 3922894]

Laurent P, Jolivel V, Manicki P, Chiu L, Contin-Bordes C, Truchetet ME, and Pradeu T (2017). Immune-Mediated Repair: A Matter of Plasticity. Front Immunol 8, 454. [PubMed: 28484454]

Lei W, Ren W, Ohmoto M, Urban JF Jr., Matsumoto I, Margolskee RF, and Jiang P (2018). Activation of intestinal tuft cell-expressed Sucnr1 triggers type 2 immunity in the mouse small intestine. Proc Natl Acad Sci U S A 115, 5552–5557. [PubMed: 29735652]

Liu TC, Naito T, Liu Z, VanDussen KL, Haritunians T, Li D, Endo K, Kawai Y, Nagasaki M, Kinouchi Y, et al. (2017). LRRK2 but not ATG16L1 is associated with Paneth cell defect in Japanese Crohn's disease patients. JCI Insight 2, e91917. [PubMed: 28352666]

Madison BB, Dunbar L, Qiao XT, Braunstein K, Braunstein E, and Gumucio DL (2002). Cis elements of the villin gene control expression in restricted domains of the vertical (crypt) and horizontal (duodenum, cecum) axes of the intestine. J Biol Chem 277, 33275–33283. [PubMed: 12065599]

Markart P, Faust N, Graf T, Na CL, Weaver TE, and Akinbi HT (2004a). Comparison of the microbicidal and muramidase activities of mouse lysozyme M and P. Biochem J 380, 385–392. [PubMed: 14977423]

Markart P, Korfhagen TR, Weaver TE, and Akinbi HT (2004b). Mouse lysozyme M is important in pulmonary host defense against Klebsiella pneumoniae infection. Am J Respir Crit Care Med 169, 454–458. [PubMed: 14617511]

McCafferty J, Muhlbauer M, Gharaibeh RZ, Arthur JC, Perez-Chanona E, Sha W, Jobin C, and Fodor AA (2013). Stochastic changes over time and not founder effects drive cage effects in microbial community assembly in a mouse model. ISME J 7, 2116–2125. [PubMed: 23823492]

Meyer K, Gellhorn A, and et al. (1947). Lysozyme in chronic ulcerative colitis. Proc Soc Exp Biol Med 65, 221. [PubMed: 20250444]

Meyer K, Gellhorn A, and et al. (1948). Lysozyme activity in ulcerative alimentary disease; lysozyme activity in chronic ulcerative colitis. Am J Med 5, 496–502. [PubMed: 18886575]

Mi H, Muruganujan A, Ebert D, Huang X, and Thomas PD (2019). PANTHER version 14: more genomes, a new PANTHER GO-slim and improvements in enrichment analysis tools. Nucleic Acids Res 47, D419–D426. [PubMed: 30407594]

Mootha VK, Lindgren CM, Eriksson KF, Subramanian A, Sihag S, Lehar J, Puigserver P, Carlsson E, Ridderstråle M, Laurila E, et al. (2003). PGC-1α-responsive genes involved in oxidative phosphorylation are coordinately downregulated in human diabetes. Nat Genet 34, 267–273. [PubMed: 12808457]

Nadjsombati MS, McGinty JW, Lyons-Cohen MR, Jaffe JB, DiPeso L, Schneider C, Miller CN, Pollack JL, Nagana Gowda GA, Fontana MF, et al. (2018). Detection of Succinate by Intestinal Tuft Cells Triggers a Type 2 Innate Immune Circuit. Immunity 49, 33–41 e37. [PubMed: 30021144]

Noben-Trauth N, Shultz LD, Brombacher F, Urban JF Jr., Gu H, and Paul WE (1997). An interleukin 4 (IL-4)-independent pathway for CD4+ T cell IL-4 production is revealed in IL-4 receptor-deficient mice. Proc Natl Acad Sci U S A 94, 10838–10843. [PubMed: 9380721]

Okayasu I, Hatakeyama S, Yamada M, Ohkusa T, Inagaki Y, and Nakaya R (1990). A novel method in the induction of reliable experimental acute and chronic ulcerative colitis in mice. Gastroenterology 98, 694–702. [PubMed: 1688816]

Oksanen J, Blanchet FG, Friendly M, Kindt R, Legendre P, McGlinn D, Minchin PR, O'Hara RB, Simpson GL, Solymos P, et al. (2019). The vegan package. Community ecology package, 25–4.

Pepys MB, Hawkins PN, Booth DR, Vigushin DM, Tennent GA, Soutar AK, Totty N, Nguyen O, Blake CC, Terry CJ, et al. (1993). Human lysozyme gene mutations cause hereditary systemic amyloidosis. Nature 362, 553–557. [PubMed: 8464497]

Pesce JT, Ramalingam TR, Mentink-Kane MM, Wilson MS, El Kasmi KC, Smith AM, Thompson RW, Cheever AW, Murray PJ, and Wynn TA (2009). Arginase-1-expressing macrophages suppress Th2 cytokine-driven inflammation and fibrosis. PLoS Pathog 5, e1000371. [PubMed: 19360123]

Png CW, Linden SK, Gilshenan KS, Zoetendal EG, McSweeney CS, Sly LI, McGuckin MA, and Florin TH (2010). Mucolytic bacteria with increased prevalence in IBD mucosa augment in vitro utilization of mucin by other bacteria. Am J Gastroenterol 105, 2420–2428. [PubMed: 20648002]

Proust B, Nahori MA, Ruffie C, Lefort J, and Vargaftig BB (2003). Persistence of bronchopulmonary hyper-reactivity and eosinophilic lung inflammation after anti-IL-5 or -IL-13 treatment in allergic BALB/c and IL-4Ralpha knockout mice. Clin Exp Allergy 33, 119–131. [PubMed: 12534560]

Pulendran B, and Artis D (2012). New paradigms in type 2 immunity. Science 337, 431–435. [PubMed: 22837519]

Quast C, Pruesse E, Yilmaz P, Gerken J, Schweer T, Yarza P, Peplies J, and Glockner FO (2013). The SILVA ribosomal RNA gene database project: improved data processing and web-based tools. Nucleic Acids Res 41, D590–596. [PubMed: 23193283]

Rael EL, and Lockey RF (2011). Interleukin-13 signaling and its role in asthma. World Allergy Organ J 4, 54–64. [PubMed: 23283176]

Ragland SA, and Criss AK (2017). From bacterial killing to immune modulation: Recent insights into the functions of lysozyme. PLoS Pathog 13, e1006512. [PubMed: 28934357]

Rakoff-Nahoum S, Paglino J, Eslami-Varzaneh F, Edberg S, and Medzhitov R (2004). Recognition of commensal microflora by toll-like receptors is required for intestinal homeostasis. Cell 118, 229–241. [PubMed: 15260992]

Randall L, Lemma F, Rodgers J, Vidal A, and Clifton-Hadley F (2010). Development and evaluation of internal amplification controls for use in a real-time duplex PCR assay for detection of Campylobacter coli and Campylobacter jejuni. J Med Microbiol 59, 172–178. [PubMed: 19833779]

Robertson BR, O'Rourke JL, Neilan BA, Vandamme P, On SL, Fox JG, and Lee A (2005). Mucispirillum schaedleri gen. nov., sp. nov., a spiral-shaped bacterium colonizing the mucus layer of the gastrointestinal tract of laboratory rodents. Int J Syst Evol Microbiol 55, 1199–1204. [PubMed: 15879255]

Robinette ML, Fuchs A, Cortez VS, Lee JS, Wang Y, Durum SK, Gilfillan S, Colonna M, and Immunological Genome C (2015). Transcriptional programs define molecular characteristics of innate lymphoid cell classes and subsets. Nat Immunol 16, 306–317. [PubMed: 25621825]

Sartor RB, and Mazmanian SK (2012). Intestinal Microbes in Inflammatory Bowel Diseases. Am J Gastroenterol Suppl 1, 15–21.

Schneider C, O'Leary CE, von Moltke J, Liang HE, Ang QY, Turnbaugh PJ, Radhakrishnan S, Pellizzon M, Ma A, and Locksley RM (2018). A Metabolite-Triggered Tuft Cell-ILC2 Circuit Drives Small Intestinal Remodeling. Cell 174, 271–284 e214. [PubMed: 29887373]

Segata N, Izard J, Waldron L, Gevers D, Miropolsky L, Garrett WS, and Huttenhower C (2011). Metagenomic biomarker discovery and explanation. Genome Biology 12.

Shimada J, Moon SK, Lee HY, Takeshita T, Pan H, Woo JI, Gellibolian R, Yamanaka N, and Lim DJ (2008). Lysozyme M deficiency leads to an increased susceptibility to Streptococcus pneumoniae-induced otitis media. BMC Infect Dis 8, 134. [PubMed: 18842154]

Silverberg MS, Cho JH, Rioux JD, McGovern DP, Wu J, Annese V, Achkar JP, Goyette P, Scott R, Xu W, et al. (2009). Ulcerative colitis-risk loci on chromosomes 1p36 and 12q15 found by genome-wide association study. Nat Genet 41, 216–220. [PubMed: 19122664]

Singh R, Balasubramanian I, Zhang L, and Gao N (2020). Metaplastic Paneth Cells in Extra-Intestinal Mucosal Niche Indicate a Link to Microbiome and Inflammation. Front Physiol 11, 280 [PubMed: 32296343]

Smallwood TB, Giacomin PR, Loukas A, Mulvenna JP, Clark RJ, and Miles JJ (2017). Helminth Immunomodulation in Autoimmune Disease. Front Immunol 8, 453. [PubMed: 28484453]

Stahl M, Tremblay S, Montero M, Vogl W, Xia L, Jacobson K, Menendez A, and Vallance BA (2018). The Muc2 mucin coats murine Paneth cell granules and facilitates their content release and dispersion. Am J Physiol Gastrointest Liver Physiol 315, G195–G205. [PubMed: 29698056]

Subramanian A, Tamayo P, Mootha VK, Mukherjee S, Ebert BL, Gillette MA, Paulovich A, Pomeroy SL, Golub TR, Lander ES, et al. (2005). Gene set enrichment analysis: a knowledge-based approach for interpreting genome-wide expression profiles. Proc Natl Acad Sci U S A 102, 15545–15550. [PubMed: 16199517]

Tailford LE, Crost EH, Kavanaugh D, and Juge N (2015a). Mucin glycan foraging in the human gut microbiome. Front Genet 6, 81. [PubMed: 25852737]

Tailford LE, Owen CD, Walshaw J, Crost EH, Hardy-Goddard J, Le Gall G, de Vos WM, Taylor GL, and Juge N (2015b). Discovery of intramolecular trans-sialidases in human gut microbiota suggests novel mechanisms of mucosal adaptation. Nature communications 6, 7624.

Tan C, Smith RP, Srimani JK, Riccione KA, Prasada S, Kuehn M, and You L (2012). The inoculum effect and band-pass bacterial response to periodic antibiotic treatment. Mol Syst Biol 8, 617. [PubMed: 23047527]

Tanaka M, Saito H, Kusumi T, Fukuda S, Shimoyama T, Sasaki Y, Suto K, Munakata A, and Kudo H (2001). Spatial distribution and histogenesis of colorectal Paneth cell metaplasia in idiopathic inflammatory bowel disease. J Gastroenterol Hepatol 16, 1353–1359. [PubMed: 11851832]

VanDussen KL, Liu TC, Li D, Towfic F, Modiano N, Winter R, Haritunians T, Taylor KD, Dhall D, Targan SR, et al. (2014). Genetic variants synthesize to produce paneth cell phenotypes that define subtypes of Crohn's disease. Gastroenterology 146, 200–209. [PubMed: 24076061]

von Moltke J, Ji M, Liang HE, and Locksley RM (2016). Tuft-cell-derived IL-25 regulates an intestinal ILC2-epithelial response circuit. Nature 529, 221–225. [PubMed: 26675736]

Wallrapp A, Riesenfeld SJ, Burkett PR, Abdulnour RE, Nyman J, Dionne D, Hofree M, Cuoco MS, Rodman C, Farouq D, et al. (2017). The neuropeptide NMU amplifies ILC2-driven allergic lung inflammation. Nature 549, 351–356. [PubMed: 28902842]

White JR, Nagarajan N, and Pop M (2009). Statistical methods for detecting differentially abundant features in clinical metagenomic samples. PLoS Comput Biol 5, e1000352. [PubMed: 19360128]

Williams JW, Tjota MY, Clay BS, Vander Lugt B, Bandukwala HS, Hrusch CL, Decker DC, Blaine KM, Fixsen BR, Singh H, et al. (2013). Transcription factor IRF4 drives dendritic cells to promote Th2 differentiation. Nat Commun 4, 2990. [PubMed: 24356538]

Willing BP, Dicksved J, Halfvarson J, Andersson AF, Lucio M, Zheng Z, Jarnerot G, Tysk C, Jansson JK, and Engstrand L (2010). A pyrosequencing study in twins shows that gastrointestinal microbial profiles vary with inflammatory bowel disease phenotypes. Gastroenterology 139, 1844–1854 e1841. [PubMed: 20816835]

Yu S, Nie Y, Knowles B, Sakamori R, Stypulkowski E, Patel C, Das S, Douard V, Ferraris RP, Bonder EM, et al. (2014). TLR sorting by Rab11 endosomes maintains intestinal epithelial-microbial homeostasis. The EMBO journal 33, 1882–1895. [PubMed: 25063677]

Yu S, Tong K, Zhao Y, Balasubramanian I, Yap GS, Ferraris RP, Bonder EM, Verzi MP, and Gao N (2018). Paneth Cell Multipotency Induced by Notch Activation following Injury. Cell Stem Cell 23, 46–59 e45. [PubMed: 29887318]

Zaiss DM, Yang L, Shah PR, Kobie JJ, Urban JF, and Mosmann TR (2006). Amphiregulin, a TH2 cytokine enhancing resistance to nematodes. Science 314, 1746. [PubMed: 17170297]

Zhang Q, Pan Y, Yan R, Zeng B, Wang H, Zhang X, Li W, Wei H, and Liu Z (2015). Commensal bacteria direct selective cargo sorting to promote symbiosis. Nat Immunol 16, 918–926. [PubMed: 26237551]

Highlights

- Abnormal production of Paneth cell lysozyme is a feature of human IBD
- Intestinal luminal lysozyme determines the abundance of mucolytic commensal bacteria
- Processing lysozyme-sensitive bacterial cell wall drives colitis in *Lyz1*$^{+/+}$ hosts
- *Lyz1*$^{-/-}$ mice have reduced NLR signaling but an anti-colitogenic type 2 immune response

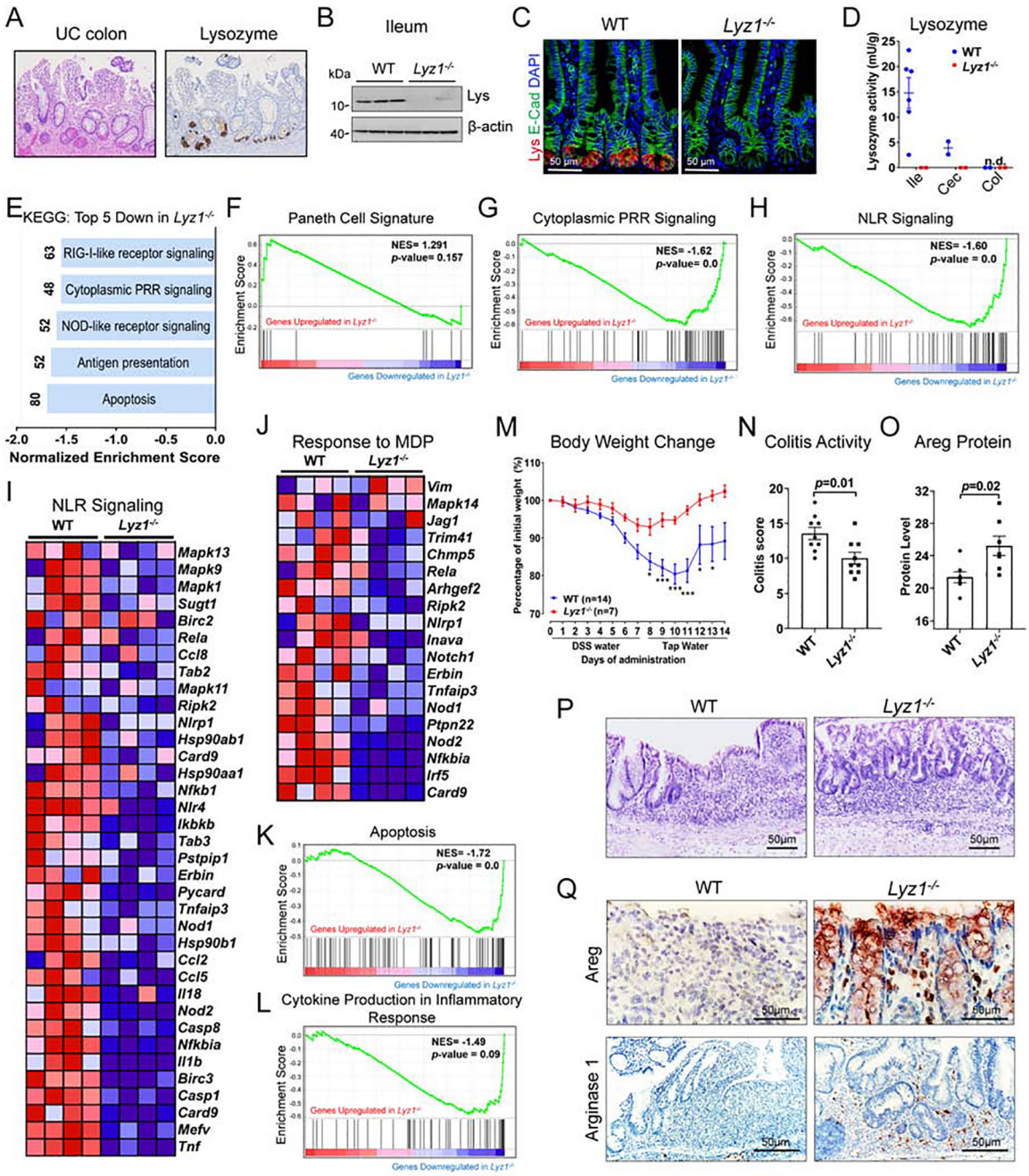

Figure 1. *Lyz1* deficiency diminishes NLR signaling and reduces inflammation during experimental colitis.

(A) Representative IBD patient left colon with metaplastic Paneth cells positive for lysozyme. **(B-C)** Loss of lysozyme protein expression in *Lyz1*$^{-/-}$ ileum by Western blotting **(B;** N=3) and by immunostaining **(C;** lysozyme in red; N>20). **(D)** Enzymatic activity of lysozyme in WT and *Lyz1*$^{-/-}$ ileum, cecum and proximal colon luminal contents was measured by a fluorometric assay (N=2–6 per genotype). **(E)** Top 5 pathways identified by KEGG analysis of differential gene expression by bulk RNAseq of WT and *Lyz1*$^{-/-}$ ileum (N=4 for each genotype for **E-L**). **(F)** No change of Paneth cell signature in *Lyz1*$^{-/-}$ ileum in

GSEA analysis. **(G-H)** Significant reduction of cytoplasmic PRR and NLR signaling in *Lyz1*$^{-/-}$ ileum in GSEA analysis (p=0.0). **(I-J)** Differenatial expression of genes involved in NLR signaling, in particular to MDP, in *Lyz1*$^{-/-}$ ileum. **(K-L)** Suppressed apoptosis and inflammatory cytokine production in *Lyz1*$^{-/-}$ ileum in GSEA analysis. **(M)** Body weight change in WT and *Lyz1*$^{-/-}$ mice during 3% DSS treatment and recovery. **(N)** Histological colitis activity scores in WT and *Lyz1*$^{-/-}$ mice after DSS treatment. **(O)** Areg protein quantitation from immune-stained sections of DSS-treated WT and *Lyz1*$^{-/-}$ mouse colons. **(P)** Representative H&E staining of the distal colons of DSS-treated WT and *Lyz1*$^{-/-}$ mice. **(Q)** Representative immunostaining of Areg and Arginase 1 in the colon of DSS-treated WT and *Lyz1*$^{-/-}$ mice. All bar graphs display mean ± SEM from at least two independent experiments. **See also** Figure S1.

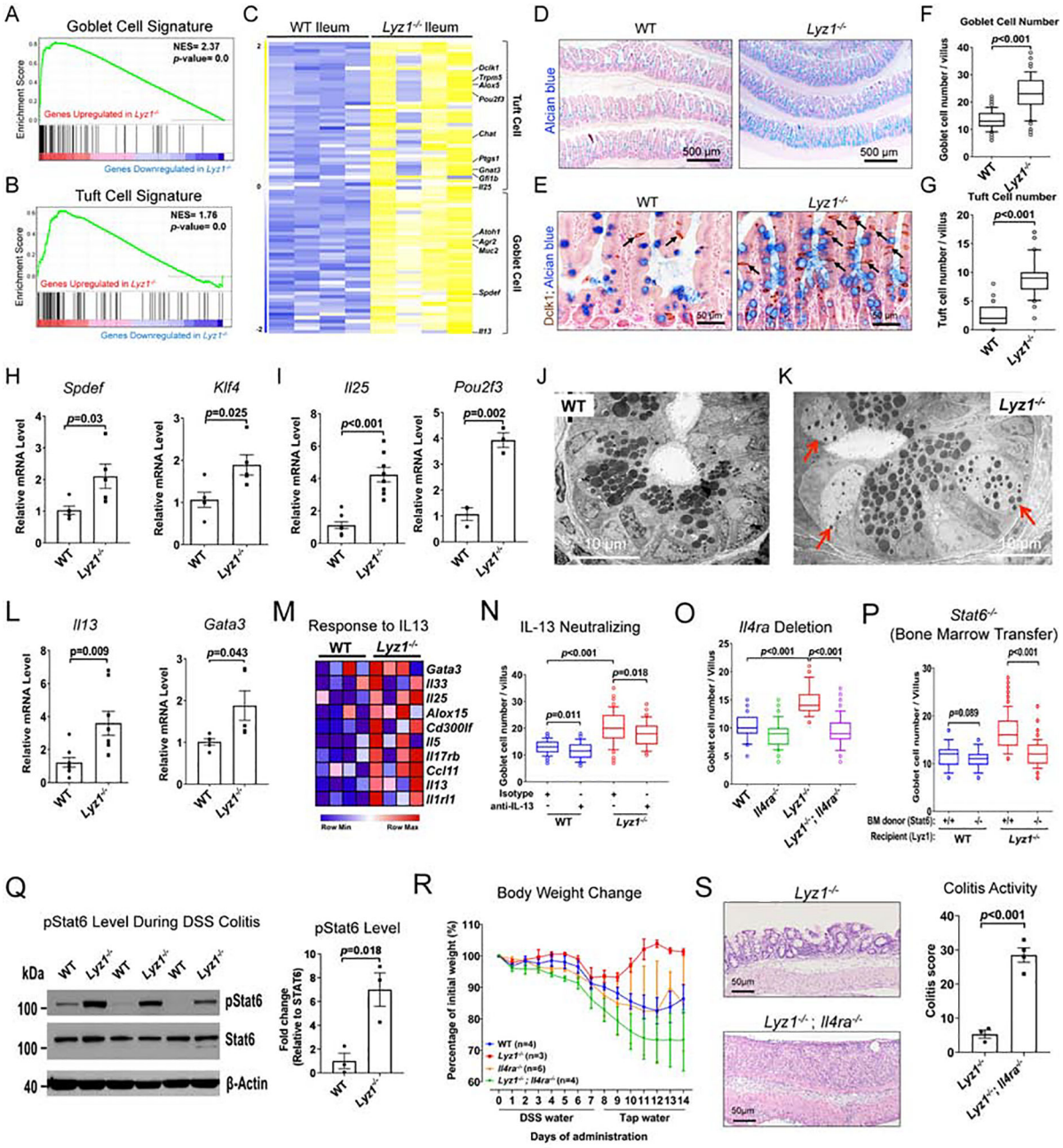

Figure 2. Elevated type 2 immune response in *Lyz1*$^{-/-}$ intestinal mucosa mediates anti-colitogenic protection.

(A-B) Elevated goblet and tuft cell signatures in *Lyz1*$^{-/-}$ ileum in GSEA analysis (p=0.0). **(C)** Differential expression of goblet and tuft cell specific genes along with IL-25 and IL-13 in WT and *Lyz1*$^{-/-}$ ileum (N=4 for each genotype). **(D-E)** Representative Alcian blue (goblet) and DCLK1 (tuft) staining in WT and *Lyz1*$^{-/-}$ ileum. **(F-G)** Quantification of the number of goblet and tuft cells per villus in WT and *Lyz1*$^{-/-}$ littermates (N=5 mice per genotype). **(H-I)** Real-time qPCR for goblet and tuft cell specific genes (N=3~6 per genotype). **(J-K)** Transmission electron microscopy of the WT and *Lyz1*$^{-/-}$ ileal crypts demonstrating cells with granules characteristic of both goblet and Paneth cells. The electron

dense granules were surrounded by expanded halos (red arrows) in abnormal Paneth cells in the *Lyz1*$^{-/-}$ (representative of N=3 for each genotype). **(L)** qPCR analysis of IL-13 and Gata3 mRNA in WT and *Lyz1*$^{-/-}$ ileum (N=3–6 for each genotype). **(M)** Differential expression of IL-13 responsive genes in WT and *Lyz1*$^{-/-}$ ileum (N=4 per genotype). **(N)** Goblet cell numbers (counted from 50 villi per field of vision per mouse) in WT or *Lyz1*$^{-/-}$ mice treated with neutralizing anti-IL-13 antibody, anti- CD90.2, or isotype control (N=2 for each condition per genotype). **(O)** Goblet cell numbers (counted from 50 villi per field of vision per mouse) in WT, *Lyz1*$^{-/-}$, *Il4*ra$^{-/-}$, or *Lyz1*$^{-/-}$; *Il4*ra$^{-/-}$ mice (N=3 for each genotype). **(P)** Goblet cell numbers (counted from 50 villi per field of vision per mouse) in WT or *Lyz1*$^{-/-}$ bone marrow chimeras with hematopietic cells from *Stat6*$^{+/+}$ or *Stat6*$^{-/-}$ donors (total N=4 mice for each condition; 2 independent experiments). **(Q)** Western blotting analysis of pStat6 from the colons of DSS-treated WT and *Lyz1*$^{-/-}$ mice (N=3 for each genotype). **(R)** Body weight change in WT, *Lyz1*$^{-/-}$, *Il4*ra$^{-/-}$, or *Lyz1*$^{-/-}$; *Il4*ra$^{-/-}$ mice treated by 3% DSS and during recovery. **(S)** Representative H&E staining and colitis histological activity score in DSS-treated *Lyz1*$^{-/-}$ and *Lyz1*$^{-/-}$; *Il4*ra$^{-/-}$ mice. All bar graphs display mean ± SEM from at least two independent experiments. **See also** Figure S2.

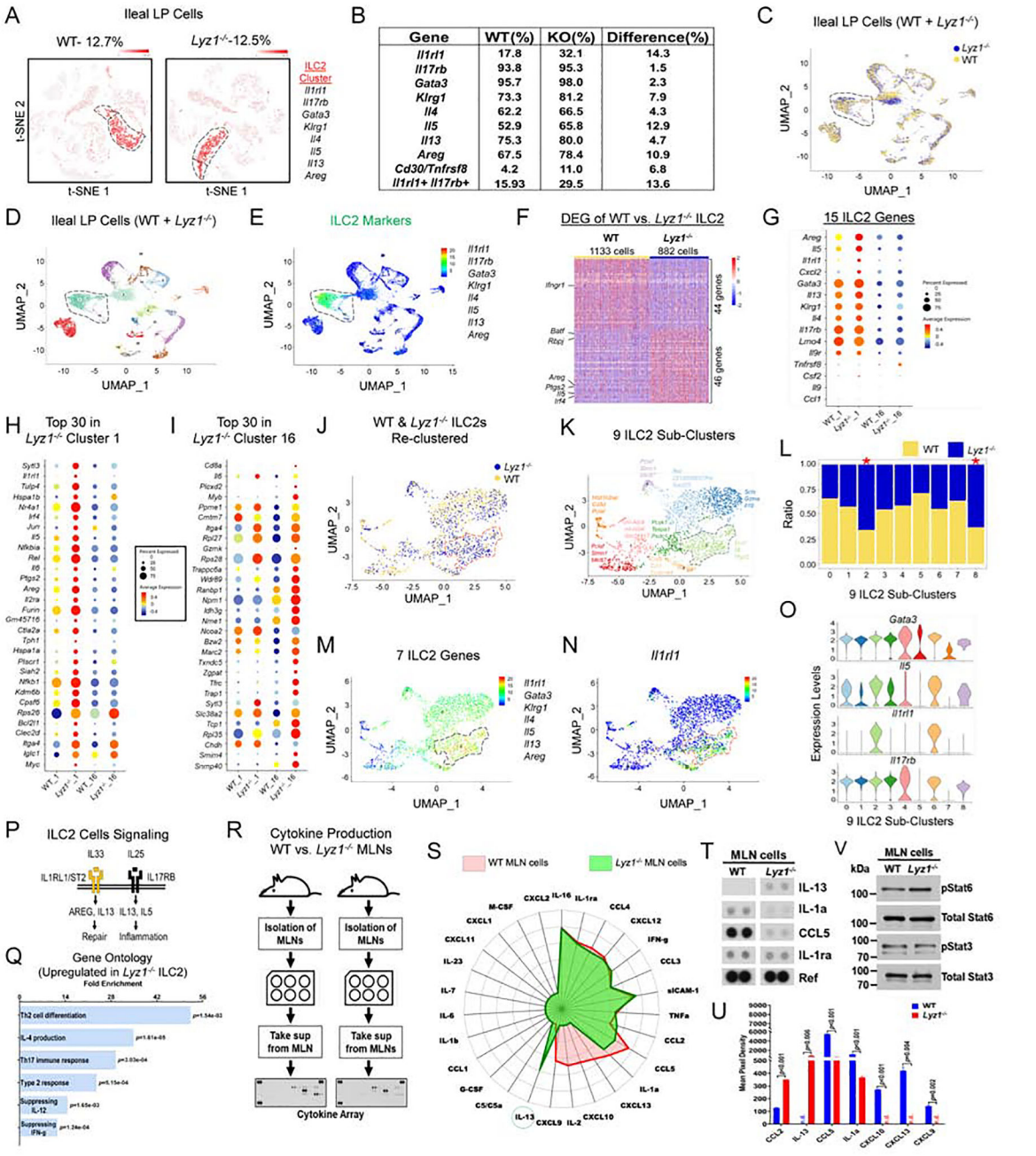

Figure 3. scRNAseq reveals immune-activated ILC2 in *Lyz1*$^{-/-}$ ileal lamina propria.

(A) Unsupervised separate clustering (t-SNE plot) of LP cells identified ILC2 populations in WT mice (total of 1,017 cells, 12.7% of all LP cells) and in *Lyz1*$^{-/-}$ mice (844 cells, 12.5% of all LP cells). **(B)** Table summarizing the percentage of ILC2 cells that expressed indicated genes in WT and *Lyz1*$^{-/-}$ LP. **(C-D)** Uniform manifold approximation and projection (UMAP) of combined clustering of WT and *Lyz1*$^{-/-}$ LP cells (WT, 8767 cells; *Lyz1*$^{-/-}$, 7492 cells) resulted in 23 distinct clusters. **(E)** ILC2s (clusters 1 &16) identified based on the indicated set of signature genes. **(F)** 90 differentially expressed genes between WT and *Lyz1*$^{-/-}$ ILC2 population in cluster 1. **(G-I)** Representative differentially expressed genes in

WT and *Lyz1*$^{-/-}$ ILC2s. Dot size reflects the percentage of cells in the cluster that express the gene; color indicates the average expression of the gene. **(G)** Differential expression of 15 ILC2 signature genes by WT and *Lyz1*$^{-/-}$ ILC2s. **(H)** Top 30 genes increased in *Lyz1*$^{-/-}$ cluster 1. **(I)** Top 30 genes increased in *Lyz1*$^{-/-}$ cluster 16. **(J-O)** All WT and *Lyz1*$^{-/-}$ ILC2 cells (a total of 2281 cells) were further partitioned into 9 sub-clusters colored by genotype **(J)** or by cluster **(K)**, with top 3 differentially expressed genes indicated next to each sub-cluster. **(L)** Bar graph with the relative distribution of WT and *Lyz1*$^{-/-}$ ILC2 cells in each sub-cluster. The *Lyz1*$^{-/-}$ ILC2-dominated sub-clusters 2 & 8 were denoted by an asterisk. **(M)** UMAP projection with 7 indicated signature genes elevated in sub-cluster 2 of *Lyz1*$^{-/-}$ ILC2. **(N)** ILC2 UMAP projection with highlighetd relative expression of Il1rl1 mRNA. **(O)** Violin plots of indicated gene expression across 9 ILC2 sub-clusters. **(P)** Schematic illustration of ILC2 signaling through IL1RL1 and IL17RB receptors in tissue repair and inflammation. **(Q)** Gene ontology (GO) categories (sorted by P value) with top pathways overrepresented in *Lyz1*$^{-/-}$ ILC2 compared to WT ILC2 in cluster 1. **(R-S)** Experimental design and radar plot with differential cytokine/chemokine secretion by WT (red) and *Lyz1*$^{-/-}$ (green) MLN cells at steady state. IL-13 highlighted by a circle. **(T)** Representative dot blots showing elevated IL-13 production by *Lyz1*$^{-/-}$ MLN cells. **(U)** Quantification of cytokine/chemokine production from two independent experiments. The bar graph displays mean ± SEM. **(V)** Western blots for pStat6 and pStat3 using MLN cell lysates from the experiment shown in S-U. **See also** Figure S3.

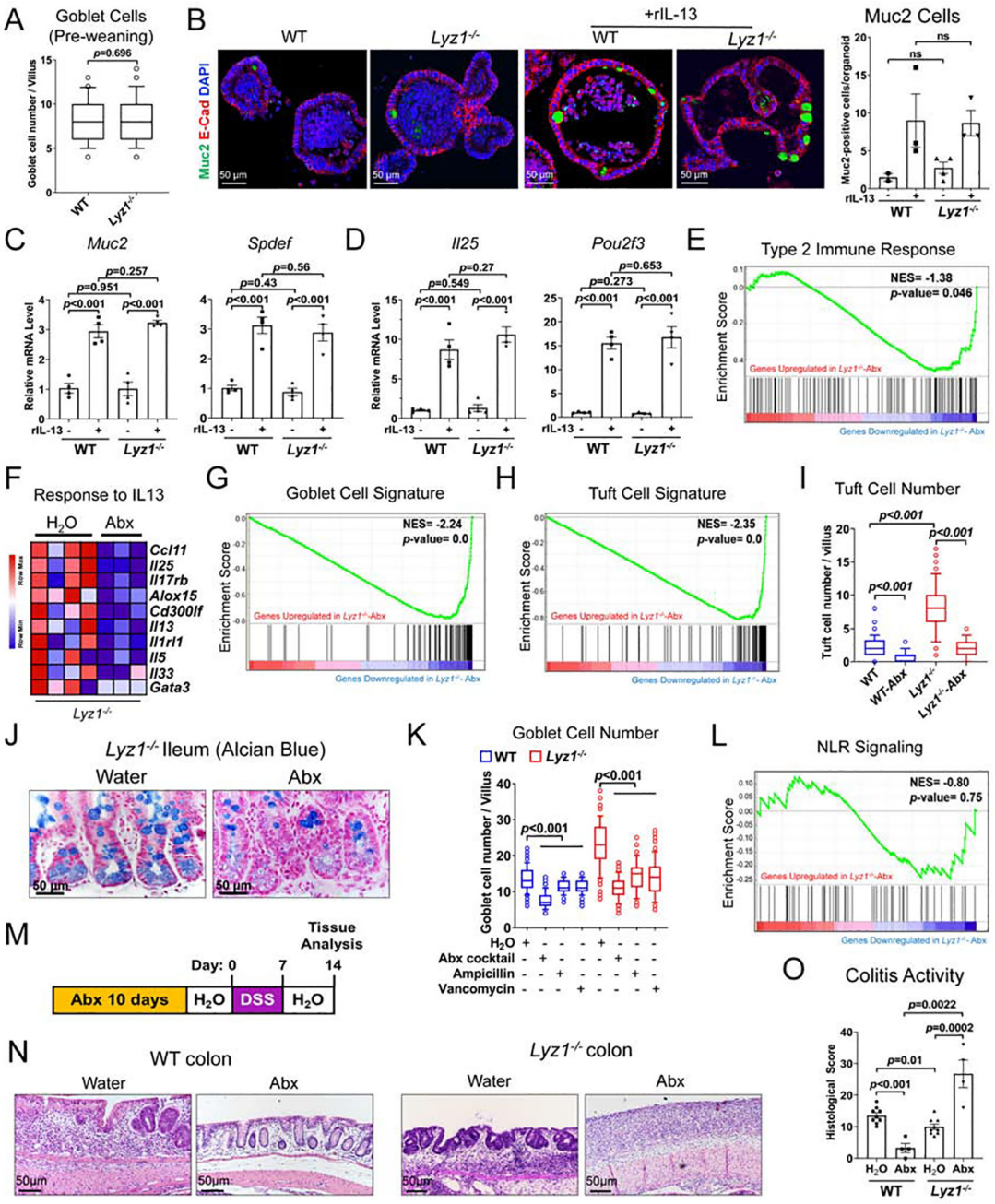

Figure 4. Altered mucosal immunity in *Lyz1*$^{-/-}$ mice is microbiota-dependent

(A) Goblet cell numbers (counted from 50 villi per field of vision per mouse) in WT or *Lyz1*$^{-/-}$ mice based on Alcian blue staining of ileal sections of 14 day-old WT and *Lyz1*$^{-/-}$ mice (N=4 for each genotype from 2 independent experiments). **(B)** The effect of genotype and IL-13 treatment on goblet cell maturation (Muc2^{+} cells in green) in ileal enteroids from WT and *Lyz1*$^{-/-}$ mice. **(C-D)** qPCR analysis of mRNA expression of goblet- and tuft cell-specific genes in ileal WT and *Lyz1*$^{-/-}$ enteroids. **(E)** GSEA analysis of genes related to type 2 immune response in the ileum of untreated or Abx-treated *Lyz1*$^{-/-}$ mice (N=3–4, bulk RNAseq). **(F)** Differential expression of IL-13-responsive genes in the ileum of untreated or

Abx-treated *Lyz1*$^{-/-}$ mice. **(G-H)** GSEA analysis of goblet and tuft cell gene signatures in the ileum of untreated or Abx-treated *Lyz1*$^{-/-}$ mice. **(I)** The effects of genotyope and Abx treatment on DCLK1^{+} tuft cell numbers (counted from 50 villi per field of vision per mouse; N=4–5 for each condition). **(J)** Representative alcian blue staining of the ileum of untreated or Abx-treated *Lyz1*$^{-/-}$ mice. **(K)** Goblet cell numbers (counted from 50 villi per field of vision per mouse) in WT or *Lyz1*$^{-/-}$ mice treated with regular water, or water with ampicillin, vancomycin, or an Abx cocktail (N=2–4 in each group). **(L)** Unaltered NLR signaling gene signature in untreated or Abx-treated *Lyz1*$^{-/-}$ mice by GSEA analysis. **(M)** Schematic of the experimental design for panels **N-O. (N-O)** Representative H&E images of distal colon and colitis activitivity scores in WT and *Lyz1*$^{-/-}$ mice treated as in panel M (N=3–7 in each group). All bar graphs display mean ± SEM from at least two independent experiments. **See also** Figure S4.

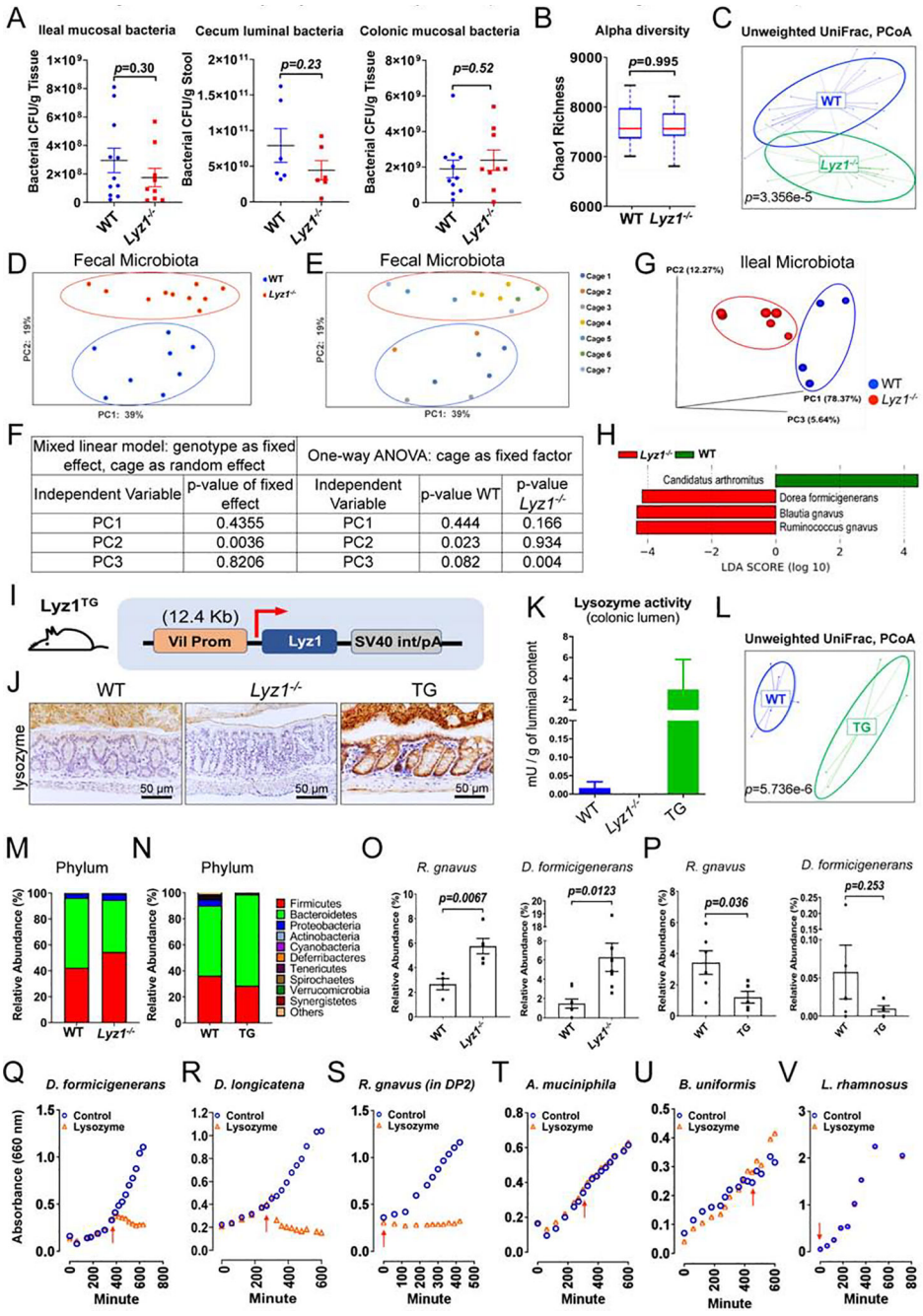

Figure 5. Paneth cell lysozyme deficiency or overproduction alters gut microbiota composition.

(A) Bacterial loads were determined in ileal and colonic mucosa and cecal lumen in WT and *Lyz1*$^{-/-}$ mice (N=6–10 in each group). **(B-H)** 16S amplicon profiling of fecal or ileal luminal microbiota from WT and *Lyz1*$^{-/-}$ mice. **(B)** Chao1 index (alpha diversity) (fecal microbiota, n=10– 12). **(C)** Unweighted UniFrac analysis of fecal microbiota from WT and *Lyz1*$^{-/-}$ mice (n=14–16). **(D-E)** PCoA analysis of fecal microbiota with consideration for genotype and cage effect (total of 8 WTs in 3 cages; 10 *Lyz1*$^{-/-}$s in 4 cages). **(F)** Mixed linear model analysis using genotype as fixed and cage as random effect. One-way ANOVA showed that cage effects contributed to differences among mice of the same genotype. **(G)**

PCoA analysis of ileal luminal microbiota from separately housed adult *Lyz1*$^{-/-}$ and WT littermates. **(H)** LDA of ileal luminal bacteria with species contracting (*Candidatus Arthromitus)* or expanding (*R. gnavus, B. gnavus, and D. formicigenerans)* in *Lyz1*$^{-/-}$mice. **(I)** Schematic diagram of the Villin-Lyz1^{TG} transgenic (TG) construct. **(J)** Lysozyme immunohistochemistry for WT, *Lyz1*$^{-/-}$, and TG mouse colons (representative of N>3 for each genotype). **(K)** Lysozyme enzymatic activity in the colonic lumen of WT, *Lyz1*$^{-/-}$, and TG mice (N=3 for each genotype). **(L)** Unweighted UniFrac analysis (16S amplicon profiling) of WT and TG mouse fecal microbiota. **(M)** Relative phyla abundance in the feces of separately housed WT and *Lyz1*$^{-/-}$ mice (N=4–8). **(N)** Relative phyla abundance of WT and TG mice (N=5–6). **(O)** Relative abundance of *R. gnavus* and *D. formicigenerans* in WT and *Lyz1*$^{-/-}$ fecal microbiota (N=4–10 per genotype). **(P)** Relative abundance of *R. gnavus* and *D. formicigenerans* in WT and TG fecal microbiota (N=5–6). **(Q-V)** Growth sensitivity of selected bacteria to lysozyme based on OD 660nm readings. Red arrowhead indicated the addition of 200 μg/ml lysozyme (data from 2–4 independent experiments). All bar graphs display mean ± SEM from at least two independent experiments. **See also** Figure S5.

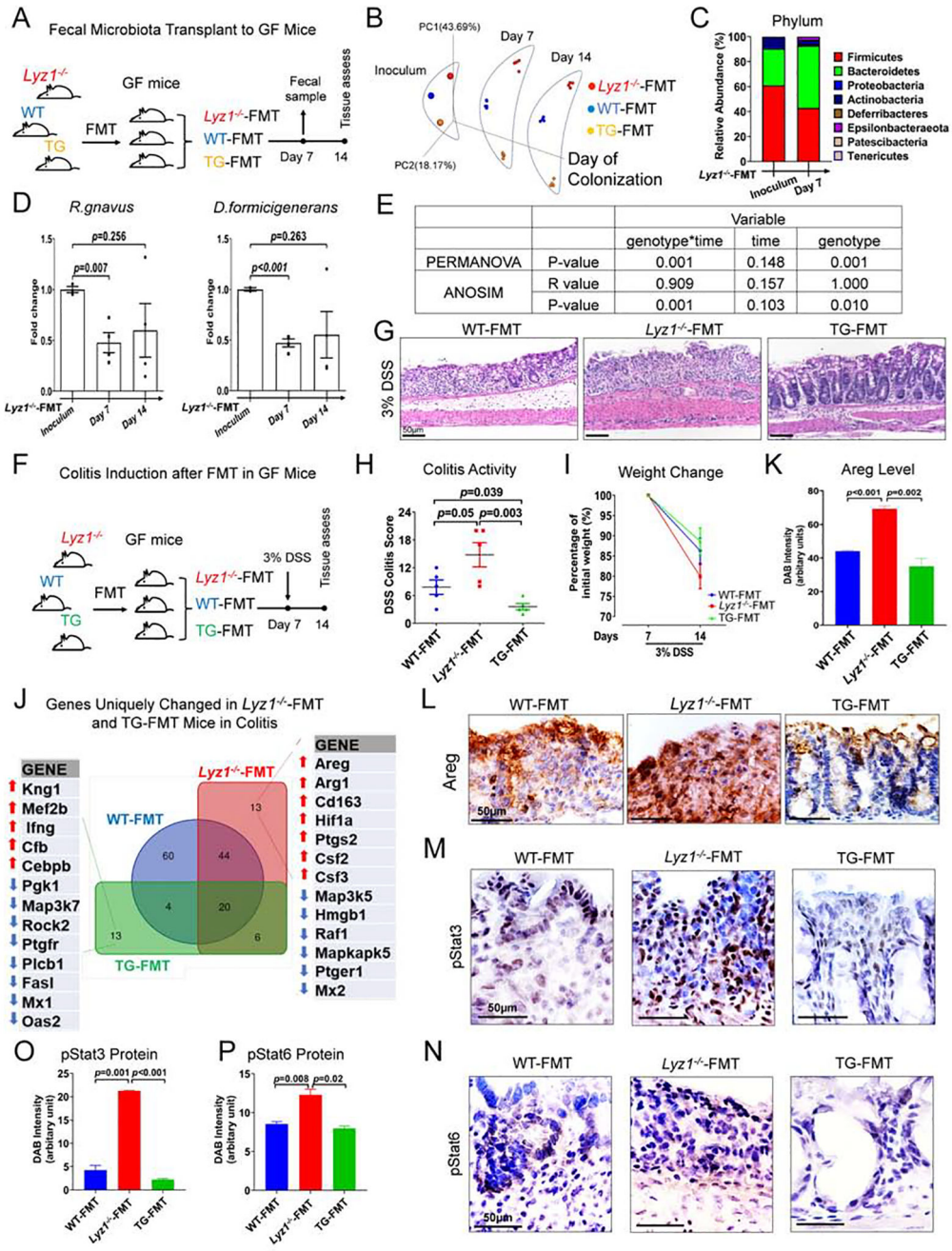

Figure 6. *Lyz1*-deficient microbiota transplanted to *Lyz1*-intact host, promotes inflammation in experimental colitis.

(A) Experimental design schematics. **(B)** PCoA showed the maintenance of diverse communities in GF mice with FMT from the 3 genotypes. **(C)** Averaged relative abundance of phyla in the *Lyz1*$^{-/-}$-FMT inoculum and in the colonized WT GF mice 7 days later. **(D)** Relative abundance of *D. formicigenerans* and *R. gnavus* in fecal microbiota of *Lyz1*$^{-/-}$-FMT mice, 7 and day 14 post-FMT as compared to inoculum. **(E)** In PERMANOVA and ANOSIM analysis, the source/genotype of the inoculum, but not the duration of colonization, determined the microbial differences. **(F)** Experimental design of DSS colitis

in ex-GF mice after FMT with different microbiota (N=5 ex-GF mice-FMT donor genotype). **(G-H)** Representative H&E images of distal colons and colitis activity scores in DSS-treated ex-GF mice. **(I)** Body weight changes of ex-GF mice before and after DSS treatment. **(J)** NanoString analysis of inflammation-related gene expression in the proximal colons of ex-GF mice before and after DSS treatment. **(K-L)** Areg immunohistochemistry in the colons of DSS-treated ex-GF mice. **(M-P)** Representative pStat3 and pStat6 immunohistochemistry and semi-quantitative analysis in the colons of DSS-treated ex-GF mice (n=5 in each group). Data are represented as mean ± SEM in **D**, **H**, **K**, **O** and **P** from at least two independent experiments. **See also** Figure S6.

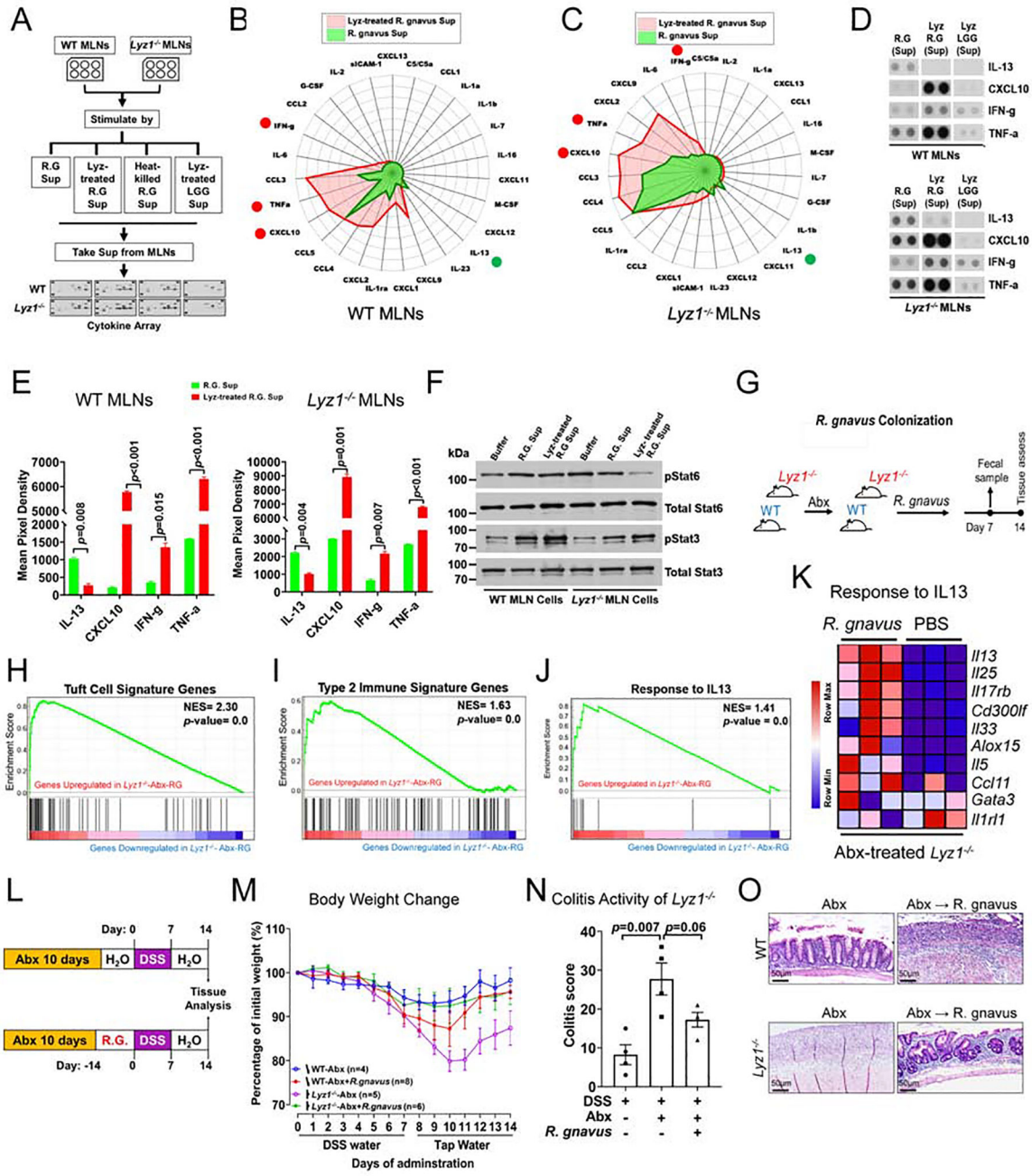

Figure 7. Distinct inflammatory cytokine induction by R. gnavus in lysozyme's presence or absence.

(A) Experimental design for data in panels B-G. **(B-C)** Radar plots of cytokine/chemokine concentrations in the media of from WT and *Lyz1*$^{-/-}$ MLN cells stimulated by supernatants from lysozyme-treated *R. gnavus* (red) versus untreated live *R. gnavus* culture (green). **(D-E)** Representative dot blots and summary quantification from two independent experiments (each in 2 replicates). **(F)** Western blots of pStat6 and pStat3 in lysates of WT and *Lyz1*$^{-/-}$ MLN cells treated analogous to B-E. **(G)** Experimental design for data in panels H-K. **(H-J)** Bulk RNAseq of ileal mucosa 14-days after *R. gnavus* gavage (n=3). Increased tuft cell

signature, type 2 immune response, and IL-13 response in *R. gnavus* colonized mice in GSEA analysis. **(K)** Differential expression of IL-13 responsive genes in *R. gnavus*-colonized *Lyz1*$^{-/-}$ compared to PBS-gavaged *Lyz1*$^{-/-}$ mice. **(L)** Experimental design for data in panels M-O showing that DSS colitis was induced in *R. gnavus* colonized WT and *Lyz1*$^{-/-}$ littermates following Abx treatment. **(M)** Body weight changes during DSS exposure and recovery in Abx-precleared WT and *Lyz1*$^{-/-}$ mice with or without *R. gnavus* association (n number indicated; 2 independent experiments). **(N)** Colitis activity scores in the colon of DSS-treated *Lyz1*$^{-/-}$ mice with or withour *R. gnavus* association. **(O)** Representative H. & E. images of DSS colons of Abx-treated and *R. gnavus* colonized WT and *Lyz1*$^{-/-}$ mice. All bar graphs display mean ± SEM. **See also** Figure S7.

KEY RESOURCES TABLE

REAGENT or RESOURCE	SOURCE	IDENTIFIER
Antibodies		
Rat anti-IL-13	R &D Systems	Cat#MAB413; RRID:AB_2124171
Rat IgG2a isotype control	R&D Systems	Cat#MAB006; RRID:AB_357349
Rabbit anti-Lysozyme	BioGenex	Cat#AR024-10R
Rabbit anti-Mucin 2 (Muc2)	Santa Cruz Biotech	Cat#sc-15334; RRID:AB_2146667
Rabbit anti-DCLK1	Abcam	Cat#ab37994; RRID:AB_873538
Goat anti-MMP7	Santa Cruz Biotech	Cat# sc-8832; RRID:AB_649337
Mouse anti-E-Cadherin (E-Cad)	BD Biosciences	Cat#610404; RRID:AB_397786
Mouse anti-Amphiregulin (Areg)	Santa Cruz Biotech	Cat# sc-74501; RRID:AB_1118939
Rabbit anti-Arginase 1	Cell Signaling	Cat#93668; RRID:AB_2800207
Rabbit anti-phospho-Stat3 (pStat3)	Cell Signaling	Cat#9145; RRID:AB_2491009
Rabbit anti-phospho-Stat6 (pStat6)	Thermo Fisher Scientific	Cat#700247; RRID:AB_2532305
Donkey anti-mouse IgG, Alexa Fluor 488	Thermo Fisher Scientific	Cat# A21202; RRID:AB_141607
Donkey anti-rabbit IgG, Alexa Fluor 568	Thermo Fisher Scientific	Cat# A10042; RRID:AB_2534017
ImmPRESS HRP anti-rabbit IgG polymer	Vector Labs	Cat# MP-7401; RRID:AB_2336529
ImmPRESS HRP anti-mouse IgG polymer	Vector Labs	Cat#MP-7402; RRID:AB_2336528
Bacterial and Virus Strains		
Akkermansia muciniphila	DSMZ	DSM-22959
Bacteroides uniformis	DSMZ	DSM-6597
Dorea formicigenerans	DSMZ	DSM-3992
Ruminococcus gnavus	DSMZ, ATCC	FRE1, ATCC29149
Lactobacillus rhamnosus GG	ATCC	ATCC53103
Dorea longicatena	DSMZ	DSM-13814
Biological Samples		
UC colon biopsy samples	Provided by Dr. Lanjing Zhang, Princeton University Hospital	N/A
CD colon and ileum biopsy samples	Provided by Dr. Lanjing Zhang, Princeton University Hospital	N/A
Chemicals, Peptides, and Recombinant Proteins		
Recombinant IL-13	R&D Systems	Cat#413-ML
Chicken egg white lysozyme	Sigma	Cat#L6876
Dextran sulfate sodium (DSS, Colitis grade)	MP Biologics	SKU 0216011080
Sodium cacodylate buffer, 0.2M, ph7.4	Electron Microscopy Sciences	Cat# 11650
8% Glutaraldehyde (EM grade)	Electron Microscopy Sciences	Cat#16019
16% Paraformaldehyde (EM grade)	Electron Microscopy Sciences	Cat#15700
4% Osmium Tetroxide (OsO4)	Electron Microscopy Sciences	Cat#19150
Proteinase Inhibitor cocktail	Roche	Cat#5892791001

REAGENT or RESOURCE	SOURCE	IDENTIFIER
Phosphatase Inhibitor cocktail	Roche	Cat#4906845001
Matrigel (growth factor reduced)	Corning	Cat#354230
IntestiCult organoid culture medium	StemCell Technologies	Cat#06005
Vector Nuclear Fast Red	Vector Labs	Cat# H-3403
EMBed-812 kit	Electron Microscopy Sciences	Cat#14120
Prolong Gold Antifade Mountant	Thermo Fisher Scientific	Cat# P36930
Hematoxylin QS	Vector Labs	Cat# H-3404
Cytoseal 60	Thermo Fisher Scientific	Cat#8310-4
4',6-Diamidino-2-Phenylindole (DAPI)	Thermo Fisher Scientific	Cat#D1306
Critical Commercial Assays		
Lysozyme activity assay kit	Abcam	Cat#ab211113
QIAamp DNA Stool Mini Kit	Qiagen	Cat#51604
PureLink Microbiome DNA purification kit	Thermo Fisher Scientific	Cat# A29789
Ion 16s Metagenomics Kit	Thermo Fisher Scientific	Cat#A26216
Cytokine array kit	R&D Systems	Cat# ARY006
Maxima First Strand cDNA Synthesis Kit	Thermo Fisher Scientific	Cat# K1641
AllPrep DNA/RNA Mini Kit	Qiagen	Cat#80204
Deposited Data		
Single-cell RNA-seq	This paper	GEO: GSE151152
Bulk-cell RNA-seq	This paper	GEO: GSE151151
Experimental Models: Organisms/Strains		
Mouse: *Lyz1*$^{H2BmCherry\text{-}IRES\text{-}CreERT2}$	Yu et al., 2018	N/A
Mouse: *Villin-Lyz1*^{TG} *transgenic*	This study	N/A
Mouse: B6.129S2(C)-Stat6^{tm1Gru}/J *(Stat6KO)*	Kaplan et al., 1996	Jax #005977
Mouse: BALB/c-Il4ra^{tm1Sz}/J (*Il4Rα KO*)	Noben-Trauth et al., 1997	Jax #003514
Oligonucleotides		
Primers for *Dorea formicigenerans*, see Table S7	Kurakawa et al., 2015	N/A
Primers for *Ruminococcus gnavus*, see Table S7	Png et al.,2010	N/A
Primers for *Bacterial 16s rRNA*, see Table S7	Randall et al., 2010	N/A
Primers for *Tritrichomonas muris*, see Table S7	Howitt et al., 2016	N/A
Primers for Mouse Lyz1, see Table S7	This paper	N/A
Primers for Mouse Mucin 2 (Muc2), see Table S7	This paper	N/A
Primers for Mouse Klf4, see Table S7	This paper	N/A
Primers for Mouse Spdef, see Table S7	This paper	N/A
Primers for Mouse Il4, see Table S7	This paper	N/A
Primers for Mouse Il13, see Table S7	This paper	N/A
Primers for Mouse Il17a, see Table S7	This paper	N/A
Primers for Mouse Il17f, see Table S7	This paper	N/A
Primers for Mouse Il25, see Table S7	This paper	N/A

REAGENT or RESOURCE	SOURCE	IDENTIFIER
Primers for Mouse Il33, see Table S7	This paper	N/A
Primers for Mouse Tslp, see Table S7	This paper	N/A
Primers for Mouse Tnfa, see Table S7	This paper	N/A
Primers for Mouse Pou2f3, see Table S7	This paper	N/A
Primers for Mouse Gata3, see Table S7	This paper	N/A
Primers for Mouse Tbx21 (Tbx), see Table S7	This paper	N/A
Primers for Mouse Rorc (Rorγt), see Table S7	This paper	N/A
Primers for Mouse Foxp3, see Table S7	This paper	N/A
Primers for Mouse Tgfb1, see Table S7	This paper	N/A
Primers for Mouse Amphiregulin (Areg), see Table S7	This paper	N/A
Primers for Mouse Hprt, see Table S7	This paper	N/A
Software and Algorithms		
Metastats	White et al., 2009	http://metastats.cbcb.umd.edu/detection.html
QIIME (v.1.9.1)	Caporaso et al., 2010	https://qiime.org
LDA Effect size (LEfSe) analysis tool	Afgan et al., 2018; Segeta et al., 2011	https://huttenhower.sph.harvard.edu/galaxy/
Kallisto	Bray et al., 2016	https://pachterlab.github.io/kallisto/
nSolver Analysis software v4.0 with the nCounter Advanced Analysis module (v.2.0.115)	NanoString Technologies	https://www.nanostring.com/products/analysis-software/nsolver
GSEA	Subramanian et al., 2005; Mootha et al., 2003	http://software.broadinstitute.org/gsea/index.jsp
GO Enrichment Analysis	Ashburner et al., 2000; Mi et al., 2019	http://geneontology.org/
Origin Pro 2019	OriginLab	https://www.originlab.com/
ImageJ	NIH	https://imagej.nih.gov/ij/
Graphpad Prism (v.7.0)	Graphpad	https://www.graphpad.com/
Cell Ranger Single Cell Software Suite (v3.0.1)	10X Genomics	https://support.10xgenomics.com/single-cell-gene-expression/software/downloads/latest
Partek Flow Software (v.9.0.20.0202)	Partek	In house license
Seurat (R toolkit)	Butler et al., 2018	https://satijalab.org/seurat v.3.1.0